ORNL/NRC/LTR-

Contract Program or Project Title:	Heavy-Section Steel Technology (HSST) Program Engineering Technology Division
Subject of this Document:	Stochastic Failure Model for the Davis-Besse RPV Head
Type of Document:	Letter Report
Authors:	P. T. Williams B. R. Bass
Date of Document:	July 2002
Responsible NRC Individual and NRC Office or Division	M. T. Kirk Division of Engineering Technology Office of Nuclear Regulatory Research

Prepared for the
U. S. Nuclear Regulatory Commission
Washington, D.C. 20555-0001
Under Interagency Agreement DOE 1886-N011-9B
NRC JCN NoY6533

OAK RIDGE NATIONAL LABORATORY
Oak Ridge, Tennessee 37831-8056
managed and operated by
UT-Battelle, LLC for the
U. S. DEPARTMENT OF ENERGY
under Contract No. DE-AC05-00OR22725

ORNL/NRC/LTR-

Stochastic Failure Model for the Davis-Besse RPV Head

P. T. Williams
B. R. Bass

Oak Ridge National Laboratory
Oak Ridge, Tennessee

Manuscript Completed – July 2002
Date Published –

Prepared for the
U.S. Nuclear Regulatory Commission
Office of Nuclear Regulatory Research
Under Interagency Agreement DOE 1886-N011-9B

NRC JCN No. Y6533

OAK RIDGE NATIONAL LABORATORY
Oak Ridge, Tennessee 37831-8063
managed and operated by
UT-Battelle, LLC for the
U. S. DEPARTMENT OF ENERGY
under Contract No. DE-AC05-00OR22725

Stochastic Failure Model for the Davis-Besse RPV Head

P. T. Williams and B. R. Bass
Oak Ridge National Laboratory
P. O. Box 2009
Oak Ridge, TN, 37831-8056

Abstract

The development of a stochastic model is described in this report in which the uncertainty associated with predictions of burst pressure for circular diaphragms using computational or analytical methods is estimated. It is postulated that the trends seen in predicting the burst pressure with nine experimental disk-burst tests (using materials, geometries, and pressure loadings relevant to the Davis-Besse analysis) will be representative of the computational predictions of the burst pressure in the Davis-Besse wastage area problem. Given a computational prediction of burst pressure for a specific configuration of the wastage area, the scaled model will provide an estimate of the cumulative probability that the true burst pressure will be less than any given service pressure.

The stochastic model was developed from the following technical bases:

(1) *experimental data* obtained during disk-burst tests with loadings, geometries, and materials relevant to the Davis-Besse pressure loading, wastage-area footprint, and cladding,

(2) nonlinear, large-deformation, elastic-plastic *discrete-element analyses* of the disk-burst tests,

(3) nonlinear, finite-strain, elastic-plastic *finite-element analyses* performed for the current study, and

(4) a *theoretical criterion* for plastic instability in a circular diaphragm under pressure loading, applied to the disk-burst tests.

The final Weibull stochastic model has the scaled form of

$$\Pr\left(P_{BP(true)} \le P\right) = F_W(P \mid P_{BP}) = \begin{cases} 1-\exp\left[-\left(\dfrac{P-P_{BP}\times 0.825}{P_{BP}\times 0.308}\right)^{2.302}\right], & (P > P_{BP}\times 0.825) \\ 0, & (P \le P_{BP}\times 0.825) \end{cases}$$

A normal distribution is also available for nonzero failure-probability estimates at pressures below the location parameter in the Weibull distribution. Given a computationally predicted burst pressure, P_{BP}, the model gives an estimate of the cumulative probability, F_W, that the true (but unknown) burst pressure $P_{BP(true)} \le P$, where P is the service pressure under consideration. As an example application, estimates are provided for a bounding calculation of the "as-found" Davis-Besse wastage area.

1. Introduction

1.1. Objective

This report presents a stochastic model of failure for the stainless steel cladding in the wastage area of the Davis-Besse Nuclear Power Station reactor pressure vessel (RPV) head. For a given internal pressure, the statistical model provides an estimate of the cumulative probability that the exposed cladding will have failed at a lower pressure. The failure mode addressed by this model is *incipient tensile plastic instability* (i.e., plastic collapse) of the cladding.

1.2. Background

The following was taken from ref. [1].

> On February 16, 2002, the Davis-Besse facility began a refueling outage that included inspection of the vessel head penetration (VHP) nozzles, which focused on the inspection of control rod drive mechanism (CRDM) nozzles, in accordance with the licensee's commitments to NRC Bulletin 2001-01, "Circumferential Cracking of Reactor Pressure Vessel Head Penetration Nozzles," which was issued on August 3, 2001. These inspections identified axial indications in three CRDM nozzles, which had resulted in pressure boundary leakage. Specifically, these indications were identified in CRDM nozzles 1, 2, and 3, which are located near the center of the RPV head. ... Upon completing the boric acid removal on March 7, 2002, the licensee conducted a visual examination of the area, which identified a large cavity in the RPV head on the downhill side of CRDM nozzle 3. Followup characterization by the ultrasonic testing indicated wastage of the low alloy steel RPV head material adjacent to the nozzle. The wastage area was found to extend approximately 5 inches downhill on the RPV head from the penetration for CRDM nozzle 3, with a width of approximately 4 to 5 inches at its widest part.

See Fig. 1. for a photograph of the Davis-Besse RPV, a schematic of a typical nuclear power reactor, and a sketch and photographs of the wastage area.

1.3. Scope

In support of the investigation by the United States Nuclear Regulatory Commission's (NRC) Office of Nuclear Regulatory Research, the Heavy-Section Steel Technology Program at Oak Ridge National Laboratory has developed a statistical model of a specific failure mode for the exposed stainless steel cladding in the cavity of the Davis-Besse RPV head. Section 2 reviews the technical bases employed in the development of the model; Section 3 presents the details of the stochastic model; Section 4 demonstrates an application of the model to the results of a bounding calculation for the "as found" condition of the wastage area; and Section 5 provides a summary and conclusions.

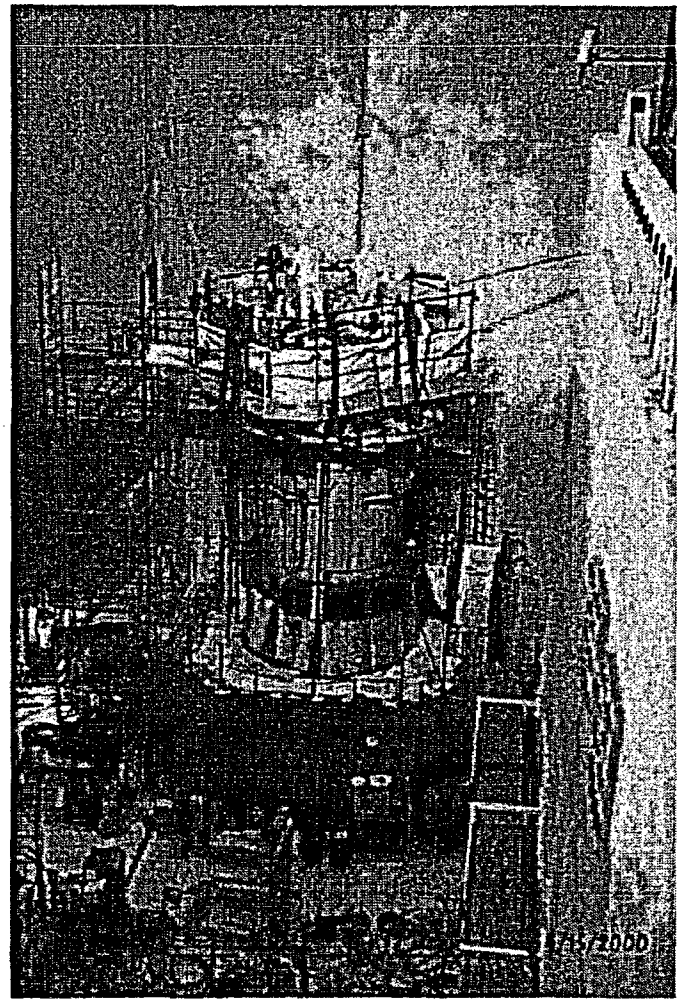

Davis Besse Reactor Vessel Head Degradation Head Cutaway View

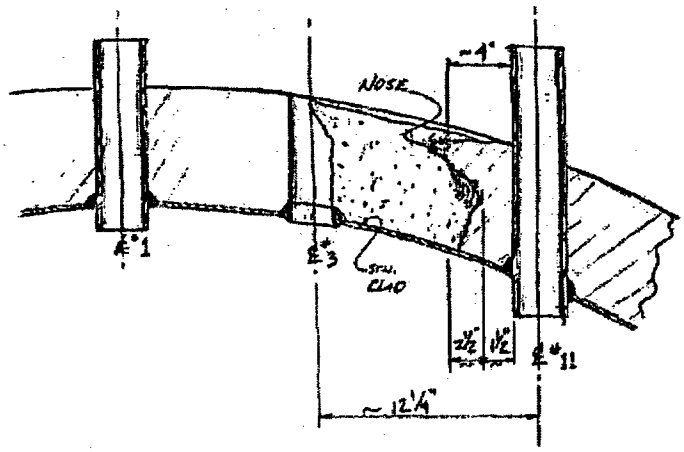

The above figure shows the Davis Besse reactor vessel head degradation between nozzle #3 and nozzle #11. This sketch was provided to the NRC by the Licensee.

Fig. 1. (a) Davis-Besse Nuclear Power Station RPV and (b) sketch of RPV head degradation.

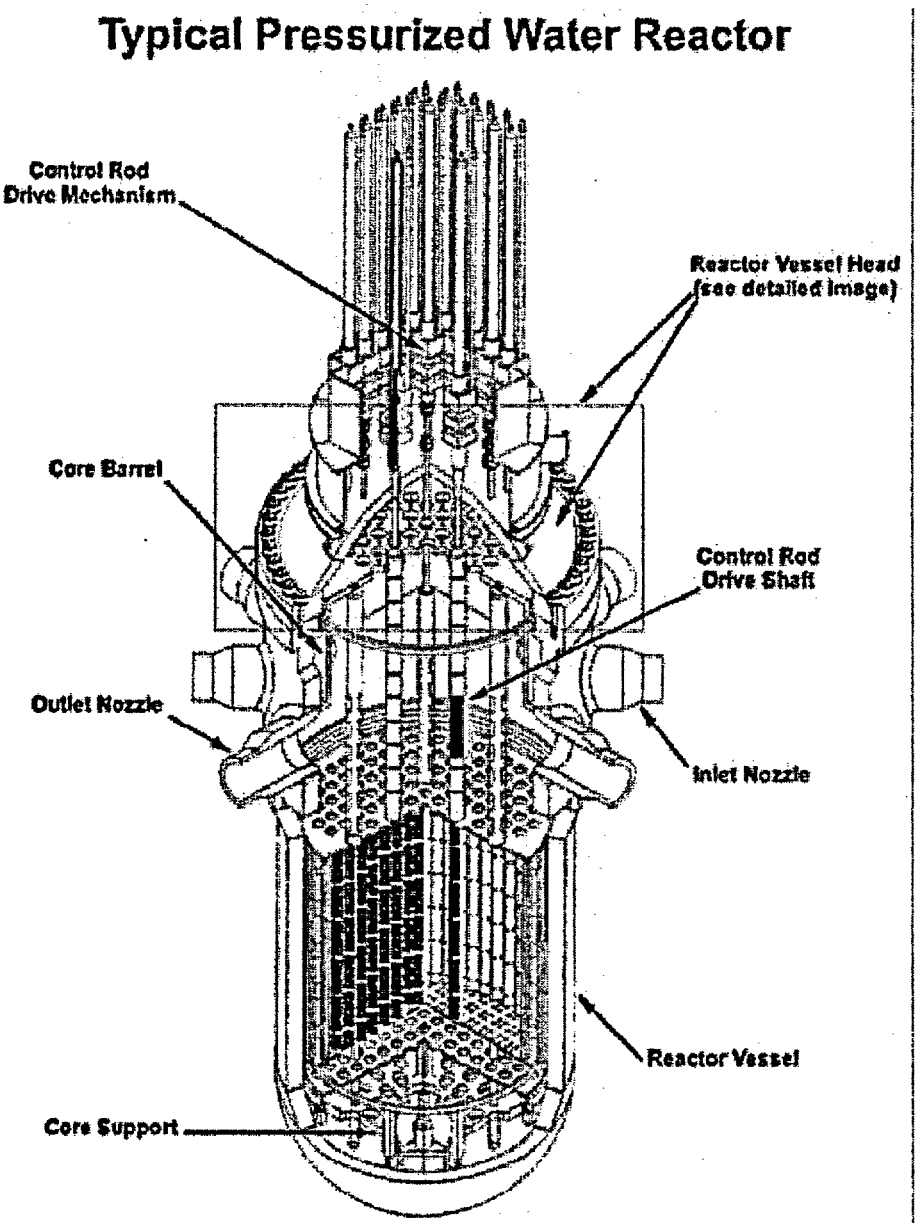

Fig. 1 (continued) (c) schematic of a typical nuclear power reactor showing the relationship of the CRDM nozzles to the RPV head.

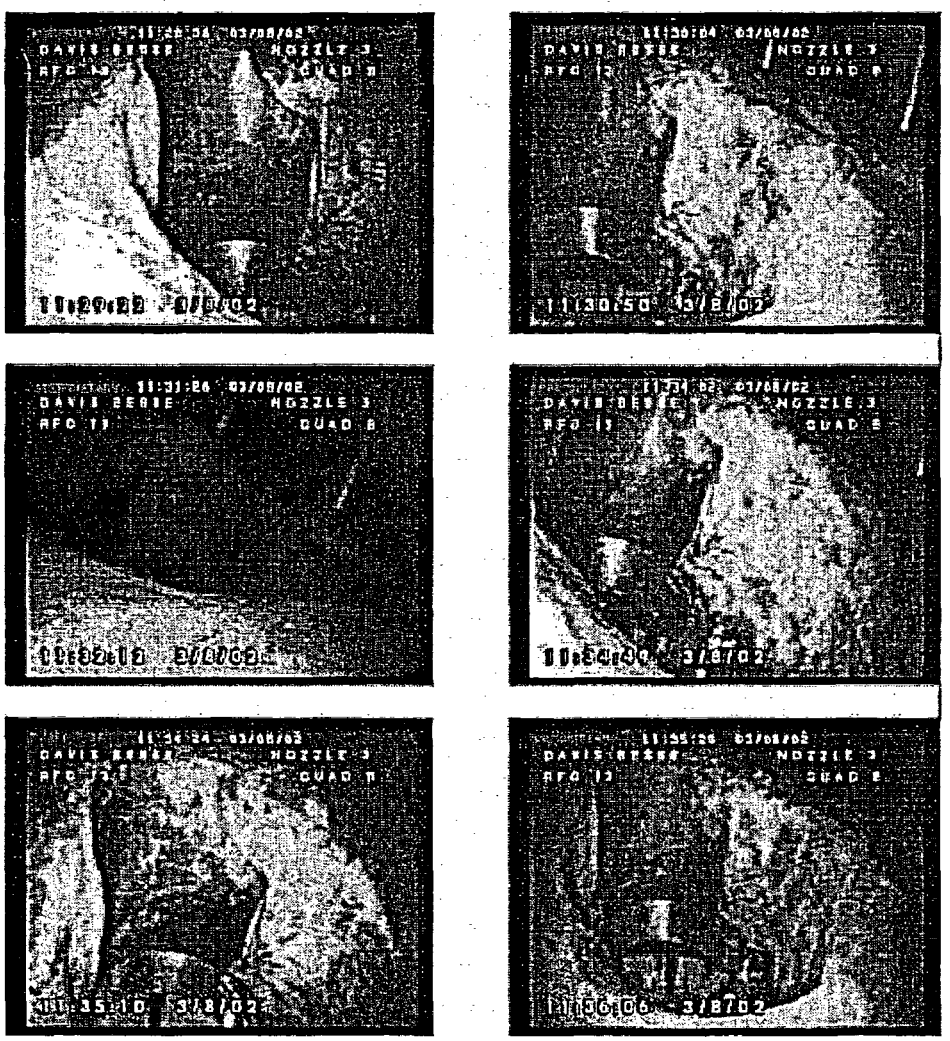

Fig. 1. (continued) (d) photographs of the wastage area with Nozzle 3 removed.

2. Technical Bases

The technical bases employed in the construction of the stochastic model are:

(1) *experimental data* obtained during disk-burst tests reported by Riccardella [2] with loadings, geometries, and materials relevant to the Davis-Besse pressure loading, wastage-area footprint, and cladding,

(2) nonlinear, large-deformation, elastic-plastic *discrete-element analyses* of the disk-burst tests also reported in [2] (GAPL-3 discrete-element code[3]),

(3) nonlinear, finite-strain, elastic-plastic *finite-element analyses* performed for the current study (ABAQUS finite-element code[4]) of the nine disk-burst test specimens reported in [2], and

(4) a *theoretical criterion* for plastic instability in a circular diaphragm under pressure loading, due to Hill [5] (as cited in [6]), applied to the disk-burst tests.

2.1. Experimental – Disk-Burst Tests

In the early 1970s, constrained disk-burst tests were carried out under the sponsorship of the ASME *PVRC Subcommittee on Effective Utilization of Yield Strength* [7]. This test program employed a range of materials and specimen geometries that were relevant to components in a nuclear power plant steam supply system[1]. The geometries of the three test specimens analyzed in [2] are shown in Fig. 2, the test matrix is shown in Table 1, and the properties of the three materials are presented in Table 2. The nine disk-burst tests produced three center failures and six edge failures over a range of burst pressures from 3.75 to 15 ksi as shown in Table 1.

Table 1. Test Matrix for Disk-burst Tests [2]

Test Number	Material	Geometry	Fillet Radius (in.)	Diaphragm Thickness (in.)	Effective Diaphragm Radius (in.)	Experimental Results: Burst Pressure (ksi)	Experimental Results: Location of Failure
1	SS 304	A	0.375	0.250	2.625	15	Edge
2		B	0.125	0.125	2.875	6.8	Center
3		C	0.375	0.125	2.625	7.7	Center
4	A533B	A	0.375	0.250	2.625	11	Edge
5		B	0.125	0.125	2.875	5.3	Edge
6		C	0.375	0.125	2.625	6.7	Center
7	ABS-C	A	0.375	0.250	2.625	9.8	Edge
8		B	0.125	0.125	2.875	3.75	Edge
9		C	0.375	0.125	2.625	4.94	Edge

[1] The three materials are representative of reactor core support structures and piping, the reactor pressure vessel, and plant component support structures [2].

Table 2. Property Data for Materials in Disk-burst Tests [2]

Material	Yield Strength 0.2% offset (ksi)	Ultimate Strength (ksi)	Strain at Ultimate (-)	True Stress 0.2% offset (ksi)	True Ultimate Stress (ksi)	Log Strain at Ultimate (-)	Power Law Fit* K (ksi)	n (-)
SS304	34	84	0.54	34.07	129.36	0.432	162.41	0.27
A-533B	74	96	0.17	74.15	112.32	0.157	139.41	0.12
ABS-C	39	64	0.31	39.08	83.84	0.270	105.20	0.17

*The power-law parameters in Table 2 were fitted for the current study where $\bar{\sigma} = K\bar{\varepsilon}^n$ and $\bar{\sigma}$, $\bar{\varepsilon}$ are the effective true stress and effective total true strain, respectively.

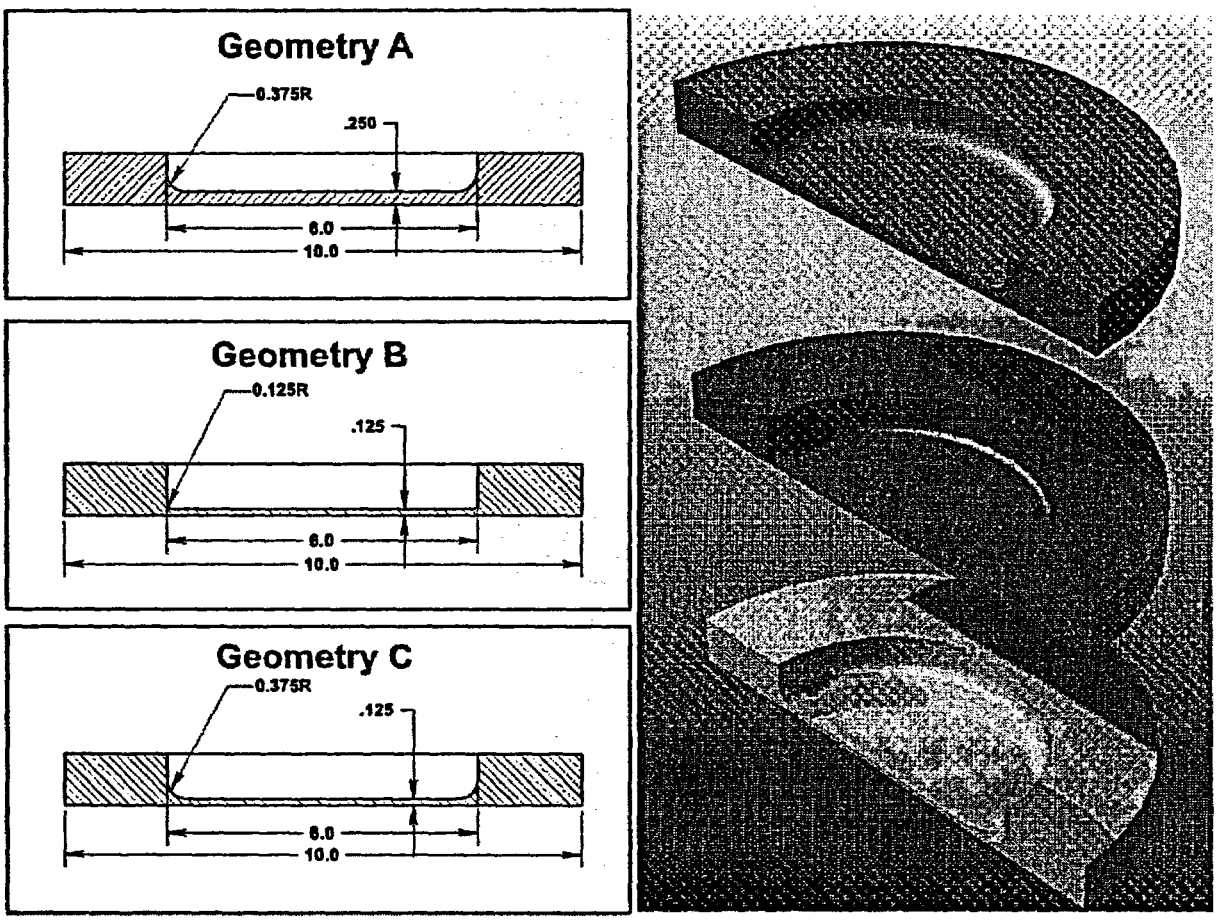

Fig. 2. Geometric descriptions of the three disk-burst specimens used in [1] (all dimensions are inches). Images on the right are Photoworks®-rendered views of ½-symmetry solid models of the three specimens.

2.2. Computational – Axisymmetric Discrete-Element and Finite-Element Models

The results of a computational study were presented in [2] in which the nine tests were simulated using the GAPL-3 computer code [3]. GAPL-3 applied the *discrete-element* method using a two-layered system of elements: one layer for the strain-displacement field and a second layer for the stress field to perform an elasto-plastic large-deformation analysis of stresses, strains, loads, and displacements of thin plates or axisymmetric shells with pressure loading. At each incremental load step, the code iterated to resolve both geometric and material nonlinearities, thus establishing a condition of static equilibrium. The GAPL-3 code did not account for the reduction in thickness of the diaphragm with increasing load, and, therefore, was unable to demonstrate the "tailing up" of the experimental center-deflection histories. As discussed in [2], the thin-shell approximation of the GAPL-3 code is not strictly valid in the fillet region. The GAPL-3 model did include a plastic-hinge type of strain redistribution, but the strain concentration effect due to the fillet radius was not accounted for, since the predicted strain distribution in the cross-section of the fillet was linear by assumption. These approximations in the analysis were driven by the limitations of the computer resources available at the time of the study in 1972.

The current study reanalyzed all nine disk-burst tests using the ABAQUS [4] finite-element code. With current computing power, many of the simplifying assumptions required in 1972 could be removed to provide a more detailed analysis. The fundamental assumptions made in the current study are:

(1) the material is assumed to be homogenous and isotropic before and throughout plastic deformation;

(2) the material is assumed to be free of pre-existing defects;

(3) the volume of the material undergoing plastic deformation is assumed to be constant (i.e., incompressible with a Poisson's ratio of 0.5);

(4) the hydrostatic component of the stress tensor has no effect on yielding; and

(5) the plastic deformation follows incremental J_2 flow theory (Mises yield criterion) with its associated flow rule (Levy-Mises) and isotropic strain hardening.

The finite-element meshes shown in Fig. 3 were developed using 8-node quadratic, axisymmetric, solid elements with reduced integration (ABAQUS element type CAX8R). The material property data given in Table 2 were used to fit power-law constitutive models for the plastic region of the three materials (see Fig. 4). The analyses applied a nonlinear finite-strain procedure with an incrementally increasing pressure load applied from zero up to the load at which numerical instabilities caused ABAQUS to abort the execution.

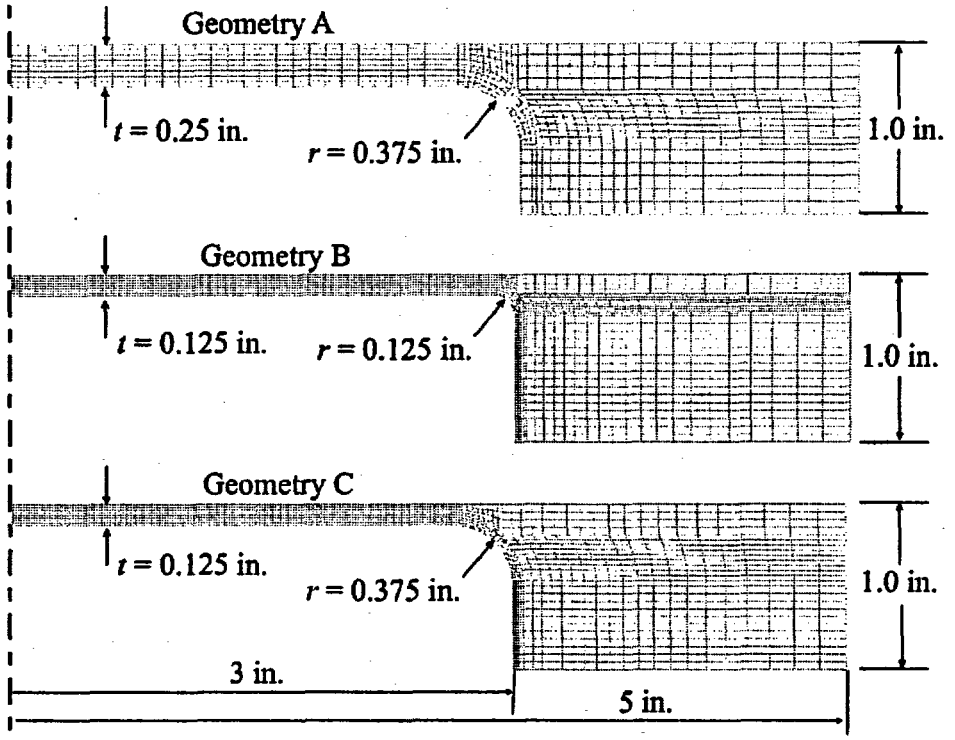

Fig. 3. Axisymmetric finite-element meshes used in the analyses of disk-burst tests reported in [2]. Quadratic 8-node axisymmetric (CAX8R) elements with reduced integration were used in a nonlinear finite-strain elastic-plastic analysis of the three disk-burst geometries with three materials.

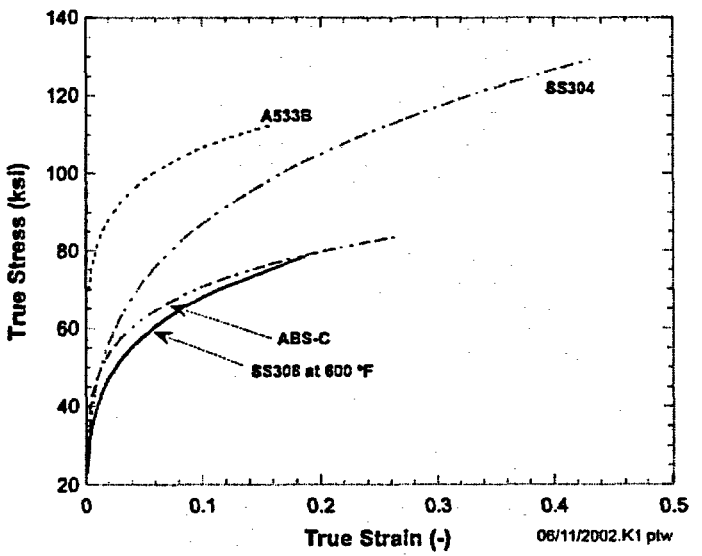

Fig. 4. True stress vs true strain curves of the three materials used in the disk-burst tests compared to SS308 at 600 °F. These three test material curves were developed using a power-law strain-hardening model fitted to yield and ultimate strength/strain data for each material given in [2]. (See Table 2).

2.3. Theory – Hill's Plastic Instability Theory

A plastic instability theory due to Hill [5] for a pressurized circular diaphragm constrained at the edges is presented in [6]. Figure 5 shows the geometry of the diaphragm, both undeformed and deformed, along with the nomenclature used in the development of the theory.

The geometry of deformation is assumed to be a spherical dome or bulge of radius, R. The undeformed ring element defined by its position, width, and thickness, $(r_0, \delta r_0, h_0)$, respectively, is assumed to deform to an axisymmetric shell element with surface length, δL, deformed thickness, h, radial position, r, and angle ϕ. The nonuniform thickness of the dome reaches its minimum at the pole with polar height H. For a spherical coordinate system with its origin at the center of the dome, the principal strains for the thin-shell (i.e., the strains are assumed constant through the thickness) element are

$$\varepsilon_\theta = \ln\left(\frac{r}{r_0}\right);\ \varepsilon_\phi = \ln\left(\frac{\delta L}{\delta r_0}\right);\ \varepsilon_h = \ln\left(\frac{h}{h_0}\right) \tag{1}$$

A geometric relationship exists between the radius and chord of a circle such that

$$R = \frac{H^2 + a^2}{2H} \tag{2}$$

where a is the effective radius of the undeformed diaphragm. Using Eqs. (1) - (2) and the geometry shown in Fig. 5, ref. [6] derives the following relations for the meridional, ε_ϕ, and hoop, ε_θ, strains at any point on the spherical bulge

$$\varepsilon_\phi(z \mid H, a) = \varepsilon_\theta(z \mid H, a) = \ln\left[1 + \left(\frac{z\,H}{a^2}\right)\right] \tag{3}$$

where the geometric parameter z is shown in Fig. 5. Applying the constant volume assumption, i.e., $\varepsilon_\phi + \varepsilon_\theta + \varepsilon_h = 0$, produces the following equation for the radial ("thickness") strain

$$\varepsilon_h(z \mid H, a) = -2\varepsilon_\phi(z \mid H, a) = \ln\left[\frac{1}{1 + \left(zH/a^2\right)}\right]^2 \tag{4}$$

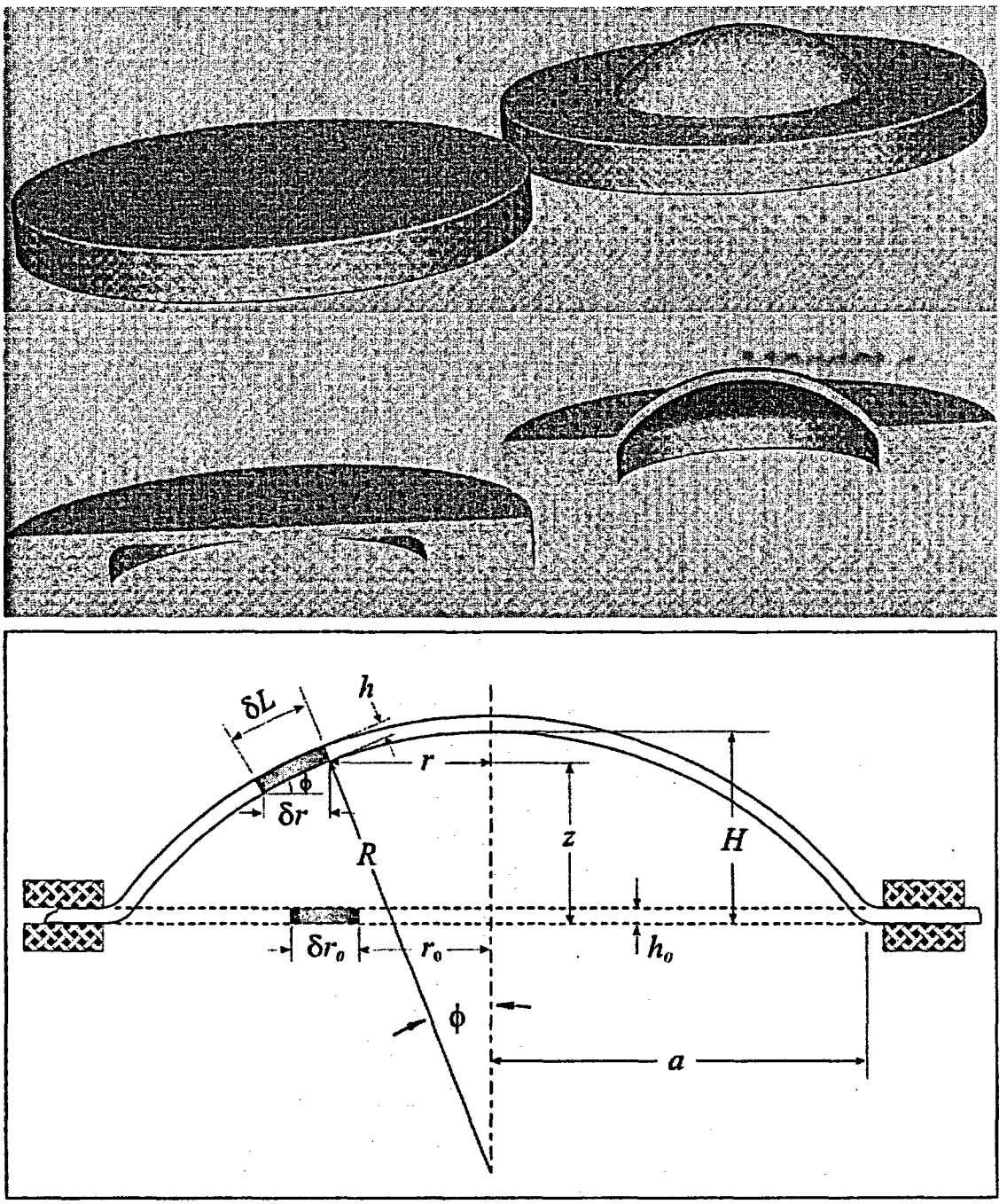

Fig. 5. Spherical geometry of deformation assumed in Hill's [5] plastic instability theory.

The effective strain then becomes

$$\bar{\varepsilon}(\varepsilon_\phi,\varepsilon_\theta,\varepsilon_h)\equiv\sqrt{\frac{2}{3}}\sqrt{(\varepsilon_\phi-\varepsilon_\theta)^2+(\varepsilon_\phi-\varepsilon_h)^2+(\varepsilon_\theta-\varepsilon_h)^2}=-\varepsilon_h(z\,|\,H,a)=2\ln\left[1+\left(\frac{z\,H}{a^2}\right)\right] \tag{5}$$

The maximum radial strain, therefore, occurs at the pole of the spherical bulge. Applying the thin-walled assumption (which is not made in the computational finite-element model) for an axisymmetric shell element, the equilibrium relation between the meridional, σ_ϕ, and hoop, σ_θ, membrane stresses and the internal pressure, p_i, loading is

$$\frac{\sigma_\phi}{R_\phi}+\frac{\sigma_\theta}{R_\theta}=\frac{p_i}{h} \tag{6}$$

For a spherical dome, $R_\theta=R_\phi=R$, and a state of equibiaxial stress is assumed to prevail near the pole of the dome with the principal stresses being

$$\sigma_\phi=\sigma_\theta=\frac{p_i R}{2h};\ \sigma_r=0 \tag{7}$$

and the effective stress, $\bar{\sigma}=\frac{1}{\sqrt{2}}\sqrt{(\sigma_\phi-\sigma_\theta)^2+(\sigma_\phi-\sigma_r)^2+(\sigma_\theta-\sigma_r)^2}$, is

$$\bar{\sigma}=\sigma_\phi=\sigma_\theta=\frac{p_i R}{2h} \tag{8}$$

To establish an instability criterion, a surface can be constructed in pressure, effective stress, and deformation/strain space by expressing Eq. (8) as a total differential of the form

$$\begin{gathered} Rp_i=2h\bar{\sigma} \\ Rdp_i+p_i dR=2hd\bar{\sigma}+2\bar{\sigma}dh \\ \frac{dp_i}{p_i}=\frac{d\bar{\sigma}}{\bar{\sigma}}+\frac{dh}{h}-\frac{dR}{R} \end{gathered} \tag{9}$$

An unstable condition exists at a point of maximum pressure on the surface where $dp_i=0$. The condition is unstable because any perturbation from this position always involves a reduction in load (pressure), even in a rising stress field. The instability criterion for a deformed bulge of radius R is, therefore, established by the following relation between stress and the deformed geometry for any point on the dome

$$\frac{d\bar{\sigma}}{\bar{\sigma}} = \frac{dR}{R} - \frac{dh}{h} \tag{10}$$

or in terms of effective strain

$$\frac{1}{\bar{\sigma}}\frac{d\bar{\sigma}}{d\bar{\varepsilon}} = 1 + \frac{1}{R}\frac{dR}{d\bar{\varepsilon}} \tag{11}$$

If the instability condition is attained, it will first occur at the point of maximum effective strain at the top of the dome (at $z = H$) such that Eq. (11) can be stated as

$$\frac{1}{\bar{\sigma}}\frac{d\bar{\sigma}}{d\bar{\varepsilon}} = \frac{3}{2} - \frac{1}{4}\left(\frac{2}{\bar{\varepsilon}}\right)\left(1 + \frac{\bar{\varepsilon}}{2}\right) \tag{12}$$

Applying a power-law constitutive form to relate effective stress to effective strain in the plastic region,

$$\bar{\sigma} = K\,\bar{\varepsilon}^{n}\ , \tag{13}$$

the effective strain at instability is, after a great deal of algebraic manipulation,

$$\bar{\varepsilon}_{crit} = \frac{4}{11}(2n+1) \tag{14}$$

where n is the power-law exponent in the constitutive equation, Eq. (13).

For a given material and diaphragm geometry (n, a, h_0), the pressure at the instability condition (i.e., the burst pressure) can be determined by the following procedure:

- Calculate the effective critical strain. $\bar{\varepsilon}_{crit} = \frac{4}{11}(2n+1)$
- Calculate the corresponding effective critical stress. $\bar{\sigma}_{crit} = K\,\bar{\varepsilon}^{n}$
- Calculate the critical thickness. $h_{crit} = h_0 \exp(-\bar{\varepsilon}_{crit})$
- Calculate the polar height at the critical condition. $H_{crit} = a\sqrt{\exp\left(\frac{\bar{\varepsilon}_{crit}}{2}\right)-1}$
- Calculate the corresponding bulge curvature radius. $R_{crit} = \frac{H_{crit}^2 + a^2}{2H_{crit}}$
- Finally, calculate the predicted burst pressure. $p_{burst} = \frac{2h_{crit}\bar{\sigma}_{crit}}{R_{crit}}$

An alternative instability criterion was developed by Chakrabarty[8] which was based on a Tresca yield surface. The critical effective strain was found to be

$$\bar{\varepsilon}_{crit} = \frac{2(2-n)(1+2n)}{11-4n} \tag{15}$$

3. Stochastic Model Development

3.1. Computational and Theoretical Model Results

Computational results using the GAPL-3 code were presented in [2]. Converged solutions were obtained for eight of the nine tests. Comparison of experimental and computational centerline deflections showed good agreement for the eight converged cases. In the nonconverged case (ABS-C, geometry C), some difficulty was reported in getting convergence at high pressures. In all cases the experimental data showed a "tailing up" as the pressure approached burst pressure, which the computational model was unable to capture. In general, the prediction of the burst pressure for the eight converged cases showed good agreement with the experimentally-determined burst pressures. Defining α as the ratio of the experimental burst pressure to the computationally-predicted burst pressure, the mean for α was 1.19 with a standard error for the mean of ± 0.0484 and a standard deviation for the sample of 0.137.

The finite-element models using ABAQUS were able to obtain burst pressures for all nine tests, where the *predicted burst pressure* is defined as the pressure at which a breakdown occurs in the numerical procedure, causing the run to abort. For a nonlinear, finite-strain, static load step, ABAQUS uses automatic sizing of the load increment to maintain numerical stability. The number of iterations needed to find a converged solution for a load increment varies depending on the degree of nonlinearity in the system. If the solution has not converged within 16 iterations or if the solution appears to diverge, ABAQUS abandons the increment and starts again with the increment size set to 25% of its previous value. An attempt is then made at finding a converged solution with this smaller load increment. If the increment still fails to converge, ABAQUS reduces the increment size again. ABAQUS allows a maximum of five cutbacks in an increment before aborting the analysis. Therefore, ABAQUS will attempt a total of 96 iterations with six increments sizes before abandoning the solution. The initial load size for the failing increment was typically already very small due to difficulties in convergence with the previous and final successfully-converged load increment.

Equivalent plastic strain contours are shown in Fig. 4 for the geometry A (ABS-C carbon steel) specimen (Test No. 7) at the point of numerical instability. The experimental burst pressure for this specimen was 9.8 ksi, and numerical instability of the solution occurred at approximately 9.05 ksi, for an $\alpha = 1.083$. Highly localized plastic straining can be observed near the fillet, thus predicting an edge failure for this specimen which did in fact fail at its edge.

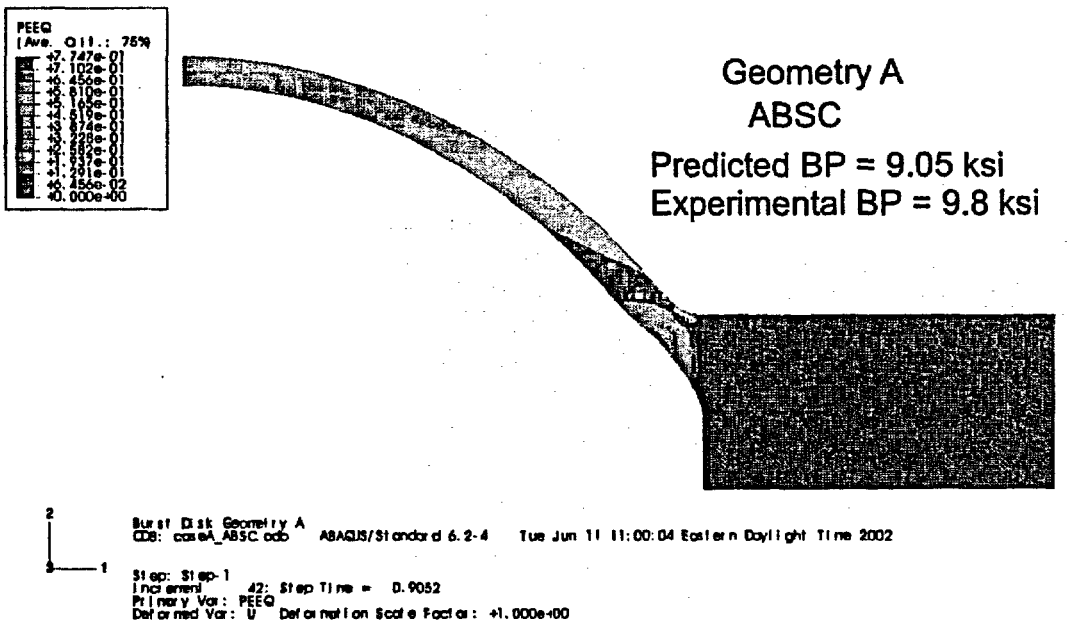

Ref. P. C. Riccardella, "Elasto-Plastic Analysis of Constrained Disk Burst Tests," ASME Paper No. 72-PVP-12, *ASME Pressure Vessels and Piping Conference*, New Orleans, LA, September 17-21, 1972.

(a)

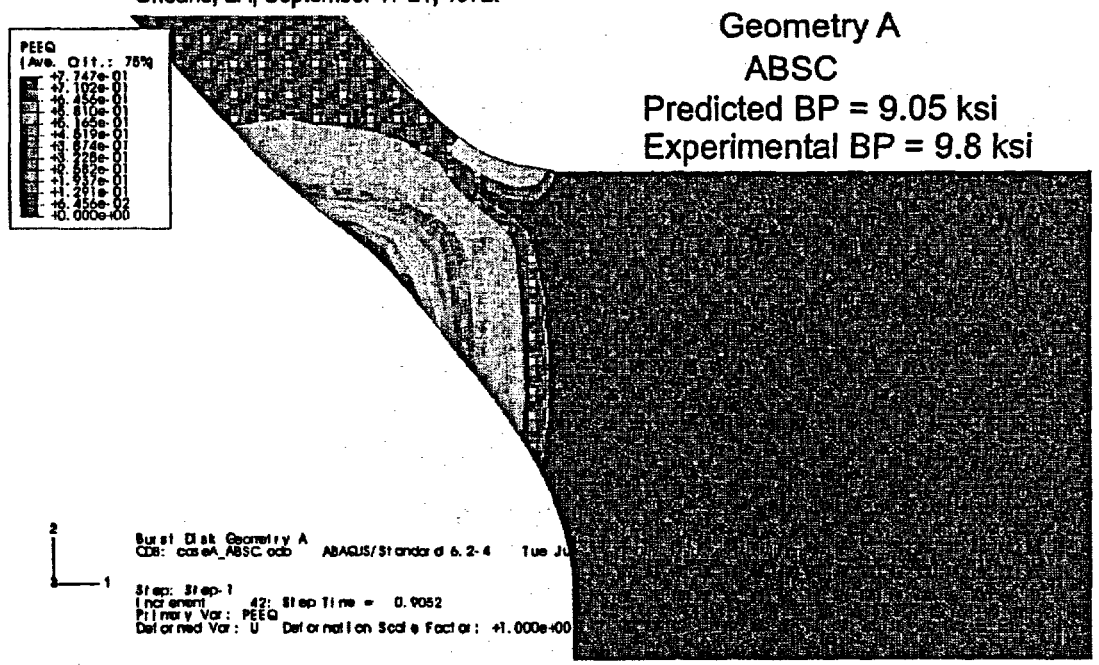

(b)

Fig. 4. Equivalent plastic strain contours for the Geometry A (ABS-C carbon steel) specimen at the point of numerical instability. Highly localized plastic straining provides a precondition for plastic collapse at the edge of the specimen. (ABAQUS analysis results)

Figure 5 compares the predicted centerline deflection load histories with the experimentally-observed deflections at failure (estimated from Figs. 3 and 4 in [2]). The "tailing up" of the experimental deflection curves near the point of failure is predicted by the model, indicating that the computational simulations are capturing the final localized "necking" of the diaphragm. For the nine ABAQUS predictions, the mean for α was 1.055 with a standard error for the mean of ±0.0331 and a standard deviation for the sample of 0.0993.

The results of applying Hill's failure criterion are presented in Table 3. The mean for α was 1.058 with a standard error for the mean of ±0.0374 and a standard deviation for the sample of 0.1123.

Table 3. Application of Hill's Instability Theory to Nine Disk-burst Tests

Test	K (ksi)	n	a (in.)	h_0 (in.)	ε_{crit}	H_{crit} (in.)	R_{crit} (in.)	σ_{crit} (ksi)	h_{crit} (in.)	P_{burst} (ksi)	$P_{burst(exp)}$ (ksi)	α
1	162.41	0.27	2.625	0.250	0.561	1.493	3.054	138.84	0.1427	12.98	15	1.156
2	162.41	0.27	2.875	0.125	0.561	1.635	3.345	138.84	0.0714	5.92	6.8	1.148
3	162.41	0.27	2.625	0.125	0.561	1.493	3.054	138.84	0.0714	6.49	7.7	1.187
4	139.41	0.12	2.625	0.250	0.449	1.316	3.276	126.96	0.1596	12.37	11	0.889
5	139.41	0.12	2.875	0.125	0.449	1.441	3.588	126.96	0.0798	5.65	5.3	0.938
6	139.41	0.12	2.625	0.125	0.449	1.316	3.276	126.96	0.0798	6.19	6.7	1.083
7	105.20	0.17	2.625	0.250	0.490	1.383	3.183	92.95	0.1532	8.95	9.8	1.095
8	105.20	0.17	2.875	0.125	0.490	1.514	3.486	92.95	0.0766	4.08	3.75	0.918
9	105.20	0.17	2.625	0.125	0.490	1.383	3.183	92.95	0.0766	4.47	4.94	1.104

A summary of all 26 burst pressure predictions is given in Table 4. Combining the 26 cases into a single sample gives a mean for α of 1.098 with a standard error for the mean of ±0.0251 and a standard deviation for the sample of 0.1281. Even though Hill's theory is applicable only for center failures, the good agreement between the experiments (including those that failed at the edges) suggests that, for the edge-failure cases, the specimens were also close to a condition of plastic collapse at the center when they failed first at the edge.

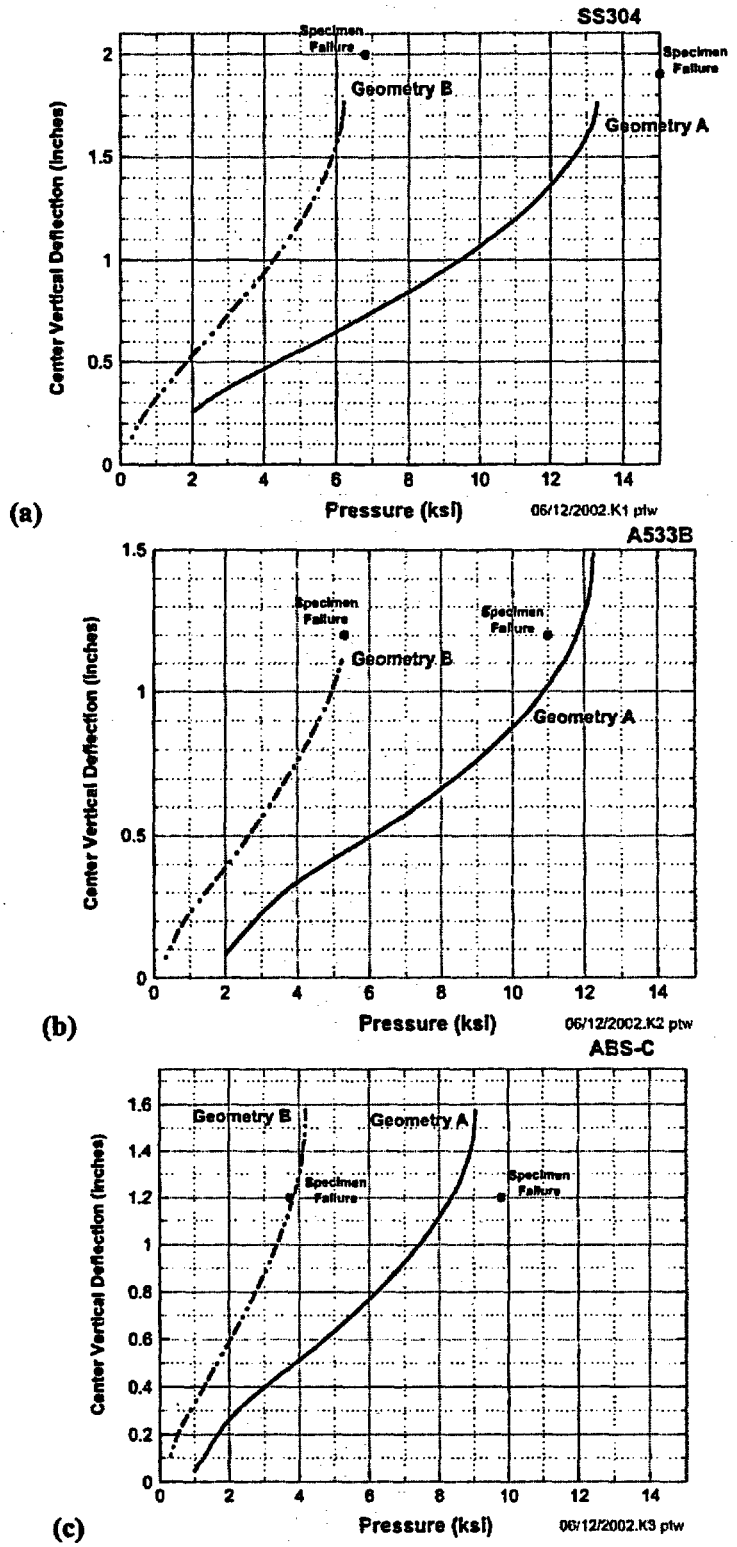

Fig. 5. Comparison of experimental centerline vertical deflections at failure to ABAQUS FEM vertical deflection histories at the center of the Geometry A and B specimens for (a) SS 304, (b) A533-B, and (c) ABS-C materials, and

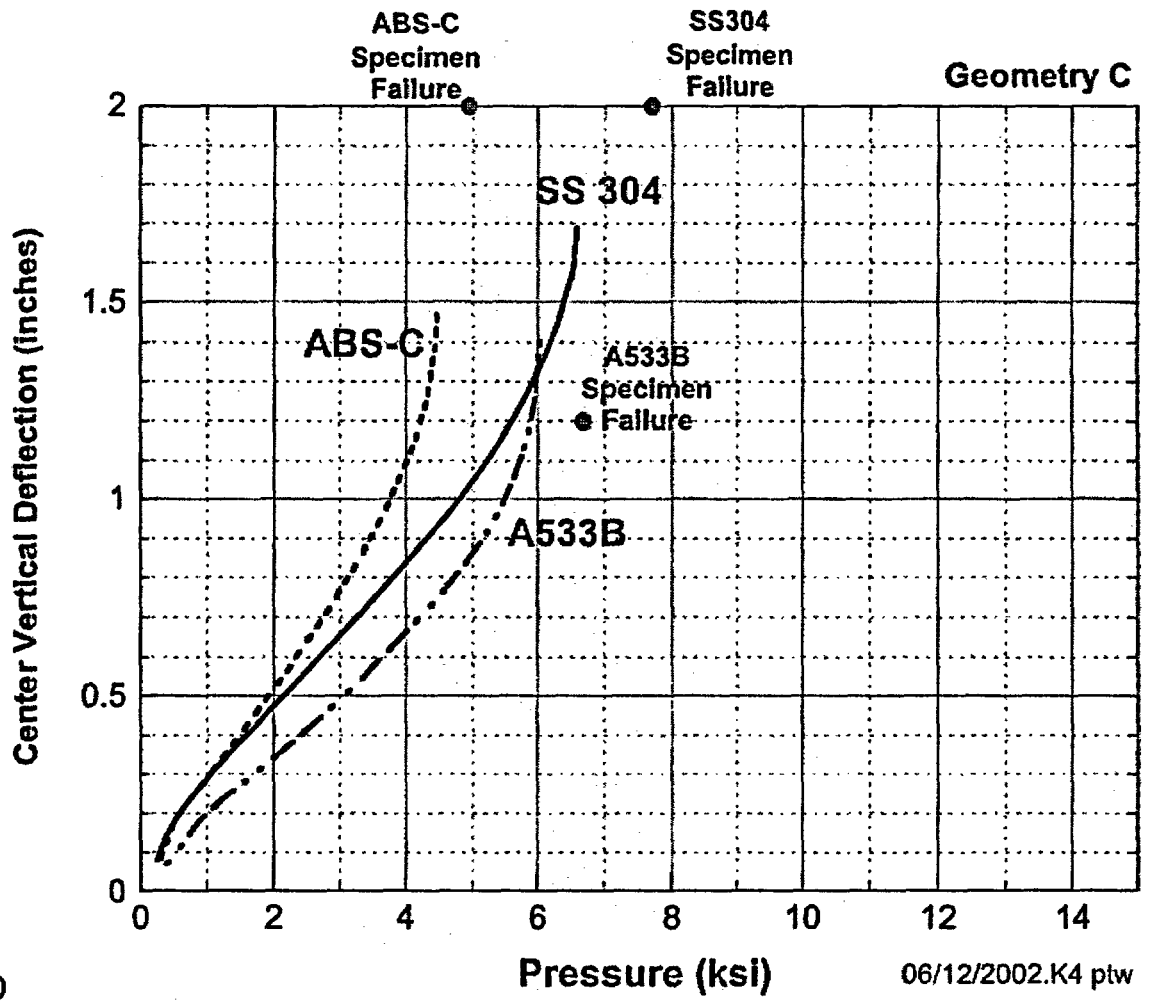

(d)

Fig. 5. (continued) (d) ABAQUS FEM vertical deflection histories at the center of Geometry C, all three materials compared to specimen failure.

Table 4. Comparison of Experimental Burst Pressures to Three Predictions

Test Number	Material	Geometry	Experimental		Riccardella's ASME Paper			Hill's Plastic Instability Theory			ABAQUS Solutions		
			Burst Pressure (BP) (ksi)	Location of Failure	Predicted Burst Pressure (BP) (ksi)	Location of Failure	Exp. BP/ Predicted BP	Predicted Burst Pressure (BP) (ksi)	Location of Failure	Exp. BP/ Predicted BP	Predicted Burst Pressure (BP) (ksi)	Location of Failure	Exp. BP/ Predicted BP
1	SS 304	A	15	Edge	12.3	Edge	1.22	12.98	Center	1.16	13.29	Edge	1.13
2		B	6.8	Center	4.8	Edge	1.42	5.92	Center	1.15	6.22	Edge	1.09
3		C	7.7	Center	7.4	Center	1.04	6.49	Center	1.19	6.59	Center	1.17
4	A533B	A	11	Edge	9.8	Edge	1.12	12.37	Center	0.89	12.26	Edge	0.90
5		B	5.3	Edge	4.2	Edge	1.26	5.65	Center	0.94	5.24	Edge	1.01
6		C	6.7	Center	6.8	Center	0.99	6.19	Center	1.08	6.03	Edge	1.11
7	ABS-C	A	9.8	Edge	8	Edge	1.23	8.95	Center	1.10	9.05	Edge	1.08
8		B	3.75	Edge	3	Edge	1.25	4.08	Center	0.92	4.19	Edge	0.89
9		C	4.94	Edge				4.47	Center	1.10	4.46	Edge/Center	1.11

3.2. Development of Stochastic Model of Failure

The development of a stochastic model is described in this section in which the uncertainty associated with predictions of burst pressure for circular diaphragms using computational or analytical methods is estimated. It is postulated that the trends observed in estimating the burst pressure with the nine disk-burst tests in [2] will be representative of the predictive accuracy of computational estimates of the burst pressure in the Davis-Besse wastage-area problem. Given a prediction of burst pressure for a specific configuration of the wastage area, the scaled stochastic model will provide an estimate of the cumulative probability that the true burst pressure will be less than a given service pressure. This postulated linkage of the test specimens to the Davis-Besse problem is obviously an approximation, since the wastage area footprints are not identical to the circular diaphragms used in the tests. The appropriateness of this linkage is in part, therefore, dependent on the ability of the finite-element models to capture, as accurately as is feasible and based on the best current knowledge, the actual geometry of the wastage area footprint.

Table 5 summarizes some descriptive statistics for the ratio of experimental burst pressure to predicted burst pressure, α, for the three predictive methods discussed in the previous section. Also shown in the table are the results of combining the three samples into one larger sample of 26 data points. Using the point estimating procedures described in the Appendix, a three-parameter Weibull distribution was fitted to the finite-element model predictions. The results of that fit are shown in Table 6 with a comparison to a normal distribution fit. The *Kolomogorov-Smirnoff* (K-S) one-sample goodness of fit statistics indicate that both models would be accepted under the null hypothesis that the sample was randomly drawn from the candidate continuous distribution. The normal distribution gives a higher K-S p-value for this sample.

A continuous three-parameter Weibull distribution has the following probability density (PDF) and cumulative distribution functions (CDF)

$$f_W(\alpha \mid a,b,c) = \frac{c}{b}\left(\frac{\alpha-a}{b}\right)^{c-1} \exp\left[-\left(\frac{\alpha-a}{b}\right)^{c}\right], \quad (\alpha > a,\ (b,c) > 0)$$
$$\Pr(X \le \alpha) = F_W(\alpha \mid a,b,c) = P = 1 - \exp\left[-\left(\frac{\alpha-a}{b}\right)^{c}\right], \ (\alpha > a,\ (b,c) > 0) \tag{16}$$

Table 5. Descriptive Statistics for the Ratio of Experimental Burst Pressure to Predicted Burst Pressures

Descriptive Statistics	Riccardella (1972)	Hill's Theory	ABAQUS	Combined
Sample Size	8	9	9	26
Mean	1.1902	1.0576	1.0549	1.0975
Standard Error	0.0484	0.0374	0.0331	0.0251
Median	1.2223	1.0953	1.0939	1.1057
Standard Deviation	0.1368	0.1123	0.0993	0.1281
Sample Variance	0.0187	0.0126	0.0099	0.0164
Kurtosis	-0.0506	-1.4799	-0.4349	0.2593
Skewness	0.0007	-0.5892	-0.9683	0.1714
Range	0.4314	0.2979	0.2739	0.5277
Minimum	0.9853	0.8889	0.8943	0.8889
Maximum	1.4167	1.1868	1.1682	1.4167
Confidence Level(95.0%)	0.1144	0.0863	0.0764	0.0517

Table 6. Weibull Model Parameters and Median Rank Order Statistics for ABAQUS Predictions

Material	Geometry	Exp. BP/ Predicted BP	Rank	Order Statistic *P*
ABS-C	B	0.89427	1	0.074
A533B	A	0.89718	2	0.181
A533B	B	1.01186	3	0.287
ABS-C	A	1.08268	4	0.394
SS 304	B	1.09393	5	0.500
ABS-C	C	1.10722	6	0.606
A533B	C	1.11041	7	0.713
SS 304	A	1.12876	8	0.819
SS 304	C	1.16822	9	0.926

Weibull Parameters		K-S *p-value* Weibull	Normal
Location	0.848	0.2928	0.4236
Scale	0.232		
Shape	2.352		
	Model	Sample	
Mean	1.0535	1.0549	
Variance	0.0087	0.0099	
Std. Dev.	0.0930	0.0993	
Median	1.0464	1.0939	

where a is the *location parameter*, b is the *scale parameter*, and c is the *shape parameter*. The inverse CDF for the Weibull distribution is given by

$$\alpha = a + b\left[-\ln(1-P)\right]^{\frac{1}{c}}; \quad 0 < P < 1 \tag{17}$$

The normal distribution function has the form

$$\begin{aligned} f_N(\alpha \mid \mu,\sigma) &= \frac{1}{\sigma\sqrt{2\pi}}\exp\left[-\frac{1}{2}\left(\frac{\alpha-\mu}{\sigma}\right)^2\right], \ (-\infty < \alpha < \infty) \\ \Pr(X \le \alpha) = F_N(\alpha \mid \mu,\sigma) &= \Phi = \int_{-\infty}^{\alpha}\frac{1}{\sigma\sqrt{2\pi}}\exp\left[-\frac{1}{2}\left(\frac{x-\mu}{\sigma}\right)^2\right]dx, \ (-\infty < \alpha < \infty) \end{aligned} \tag{18}$$

Combining the three sets into a single sample gives a sample size large enough that additional *goodness of fit statistical tests* may be carried out. Table 7 shows a ranking of the 26 data points with the median rank order statistic given by

$$P_{(i)} = \frac{i-0.3}{n+0.4} \tag{19}$$

Also given in Table 7 are the results of a χ^2 goodness of fit test comparing the Weibull distribution fitted for the combined data set with a normal distribution. The χ^2 statistics were calculated using 5 intervals with 2 degrees of freedom. The resulting p-values shown in the table indicate that both distributions would be accepted by the *null hypothesis* for the test; however, the Weibull fit has a higher confidence level of 42.9% compared to 7.6% for the normal distribution.

The combined dataset was also fitted to two-parameter gamma and log-normal distributions with the results shown in Table 8. Marginal univariate tests using the three empirical distribution function (EDF) statistics of Anderson-Darling, Cramer-von Mises, and Watson were calculated using the GenStat® program [9]. For each univariate test, the test statistics are empirical distribution function (EDF) statistics that compare the empirical distribution function of the sample with the theoretical distributions expected under the *null hypothesis*. These tests provide good power against a wide range of alternatives [10, 11]. The parameters for all four distributions were estimated by GenStat® using maximum likelihood estimators. The univariate test results in Table 8 give the Weibull distribution a *significance level* of approximately 10% (confidence level of 90%) with the other three distributions having acceptable but lower confidence levels; therefore, all four distributions would be accepted by the *null hypothesis* with the

Weibull distribution indicating a better fit to the data. Figure 6 presents GenStat® probability-probability (P-P) plots of the four distributions with order statistics given by $(i\text{-}0.5)/n$. A qualitative comparison between the plots in Fig. 6 indicates only minor differences between the distributions.

Table 7. Weibull Model Parameters and Median Rank Order Statistics for Combined Predictions

Rank	Method	Material	Geometry	α^*	Order Statistic
1	Hill's Theory	A533B	A	0.8889	0.0265
2	ABAQUS Soln.	ABS-C	B	0.8943	0.0644
3	ABAQUS Soln.	A533B	A	0.8972	0.1023
4	Hill's Theory	ABS-C	B	0.9180	0.1402
5	Hill's Theory	A533B	B	0.9382	0.1780
6	Ricardella (1972)	A533B	C	0.9853	0.2159
7	ABAQUS Soln.	A533B	B	1.0119	0.2538
8	Ricardella (1972)	SS 304	C	1.0405	0.2917
9	ABAQUS Soln.	ABS-C	A	1.0827	0.3295
10	Hill's Theory	A533B	C	1.0829	0.3674
11	ABAQUS Soln.	SS 304	B	1.0939	0.4053
12	Hill's Theory	ABS-C	A	1.0953	0.4432
13	Hill's Theory	ABS-C	C	1.1042	0.4811
14	ABAQUS Soln.	ABS-C	C	1.1072	0.5189
15	ABAQUS Soln.	A533B	C	1.1104	0.5568
16	Ricardella (1972)	A533B	A	1.1224	0.5947
17	ABAQUS Soln.	SS 304	A	1.1288	0.6326
18	Hill's Theory	SS 304	B	1.1479	0.6705
19	Hill's Theory	SS 304	A	1.1560	0.7083
20	ABAQUS Soln.	SS 304	C	1.1682	0.7462
21	Hill's Theory	SS 304	C	1.1868	0.7841
22	Ricardella (1972)	SS 304	A	1.2195	0.8220
23	Ricardella (1972)	ABS-C	A	1.2250	0.8598
24	Ricardella (1972)	ABS-C	B	1.2500	0.8977
25	Ricardella (1972)	A533B	B	1.2619	0.9356
26	Ricardella (1972)	SS 304	B	1.4167	0.9735

$^*\alpha$ = Experimental Burst Pressure/Predicted Burst Pressure

Weibull Parameters			$\chi 2$ Significance Test		
Location	0.825	Distr.	$\chi 2$	*p-value*	DOF
Scale	0.308	Normal	5.16240	0.07568	2
Shape	2.301	Weibull	1.69430	0.42864	2
	Model	Sample			
Mean	1.0975	1.0975			
Variance	0.0158	0.0164			
Std. Dev.	0.1256	0.1281			
Median	1.0876	1.1057			

Table 8. Marginal Univariate Tests for Four Distributions for Combined Sample

Distribution	Parameters		Anderson-Darling	Cramer-von Mises	Watson
Normal	mean =	1.098	0.44	0.061	0.061
	standard deviation =	0.128			
Gamma	shape =	75.82	0.501	0.073	0.072
	scale =	0.01448			
Log-Normal	log-mean =	0.0867	0.546	0.082	0.08
	log-stdev =	0.1153			
	location =	0.825			
Weibull	scale =	0.308	0.652	0.103	0.0997
	shape =	2.302			

Table 9. Critical Values of Marginal EDF Test Statistics

Test Statistic	Significance Level 15%	10%	5%	2.50%	1%
Anderson-Darling	0.576	0.656	0.787	0.918	1.092
Cramer-von Mises	0.091	0.104	0.126	0.148	0.178
Watson	0.085	0.096	0.116	0.136	0.163

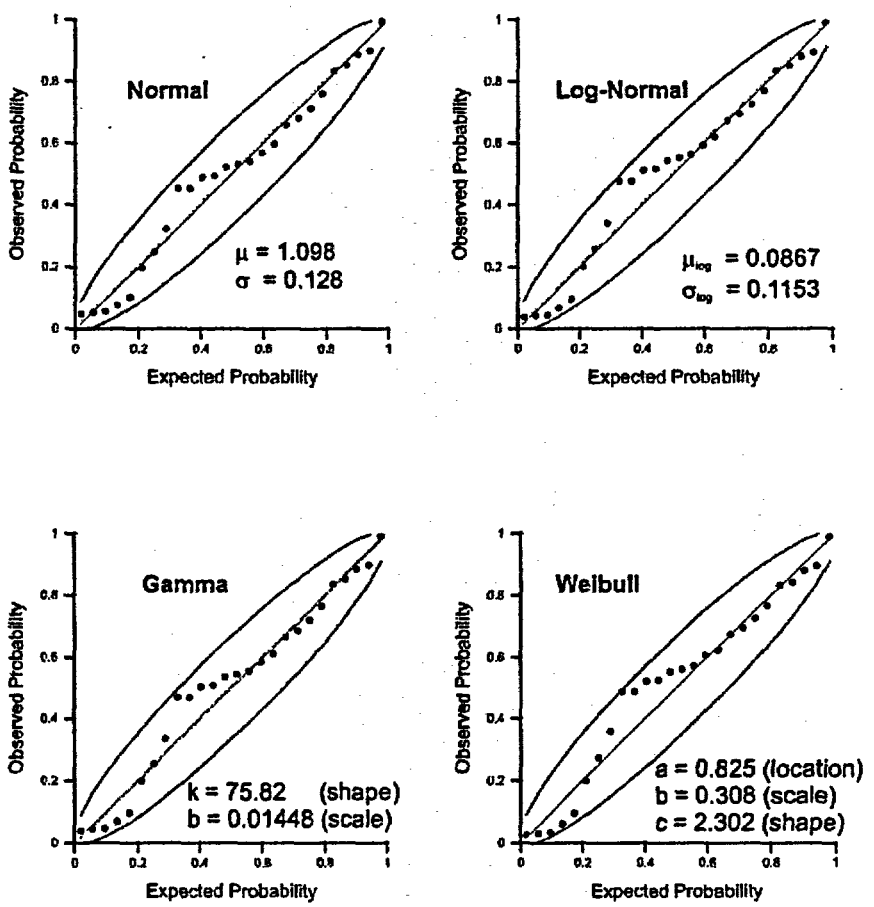

Fig. 6. GenStat® P-P plots of four distributions fitted to combined data set.

For completeness, the continuous two-parameter lognormal distribution is given by

$$f_N(\alpha \mid \mu_{\log}, \sigma_{\log}) = \frac{1}{\sigma_{\log}\alpha\sqrt{2\pi}} \exp\left[-\frac{1}{2}\left(\frac{\ln(\alpha)-\mu_{\log}}{\sigma_{\log}}\right)^2\right], \quad (-\infty < \alpha < \infty)$$
$$\Pr(X \le \alpha) = F_N(\alpha \mid \mu_{\log}, \sigma_{\log}) = \Phi = \int_{-\infty}^{\alpha} \frac{1}{\sigma_{\log} x\sqrt{2\pi}} \exp\left[-\frac{1}{2}\left(\frac{\ln(x)-\mu_{\log}}{\sigma_{\log}}\right)^2\right] dx, \quad (-\infty < \alpha < \infty) \tag{20}$$

and the two-parameter gamma distribution is described by

$$f_\Gamma(\alpha \mid b, c) = \frac{1}{b}\left(\frac{\alpha}{b}\right)^{c-1}\left[\frac{\exp\left(-\frac{\alpha}{b}\right)}{\Gamma(c)}\right], \quad (-\infty > \alpha > \infty, \; b > 0)$$
$$\Pr(X \le \alpha) = F_\Gamma(\alpha \mid b, c) = P = \int_{-\infty}^{\alpha} \frac{1}{b}\left(\frac{x}{b}\right)^{c-1}\left[\frac{\exp\left(-\frac{x}{b}\right)}{\Gamma(c)}\right] dx, \quad (b > 0) \tag{21}$$

where b is a scale parameter and c is the shape parameter.

Figure 7 compares the probability density functions of the four models to the histogram for the combined data set, and Figs. 8 and 9 show the probability density and cumulative distribution functions for the Weibull and normal models fitted to the $n = 9$ sample of FEM predictions. The corresponding PDF and CDF plots for the Weibull and normal models fitted to the combined sample of $n = 26$ are given in Figs. 10 and 11. From these results, it was decided to concentrate on the Weibull and normal distributions. These two distributions will produce bounding estimates on the conditional probability of failure for low pressures relative to the predicted burst pressure with the Weibull distribution being recognized as giving the better fit to the data.

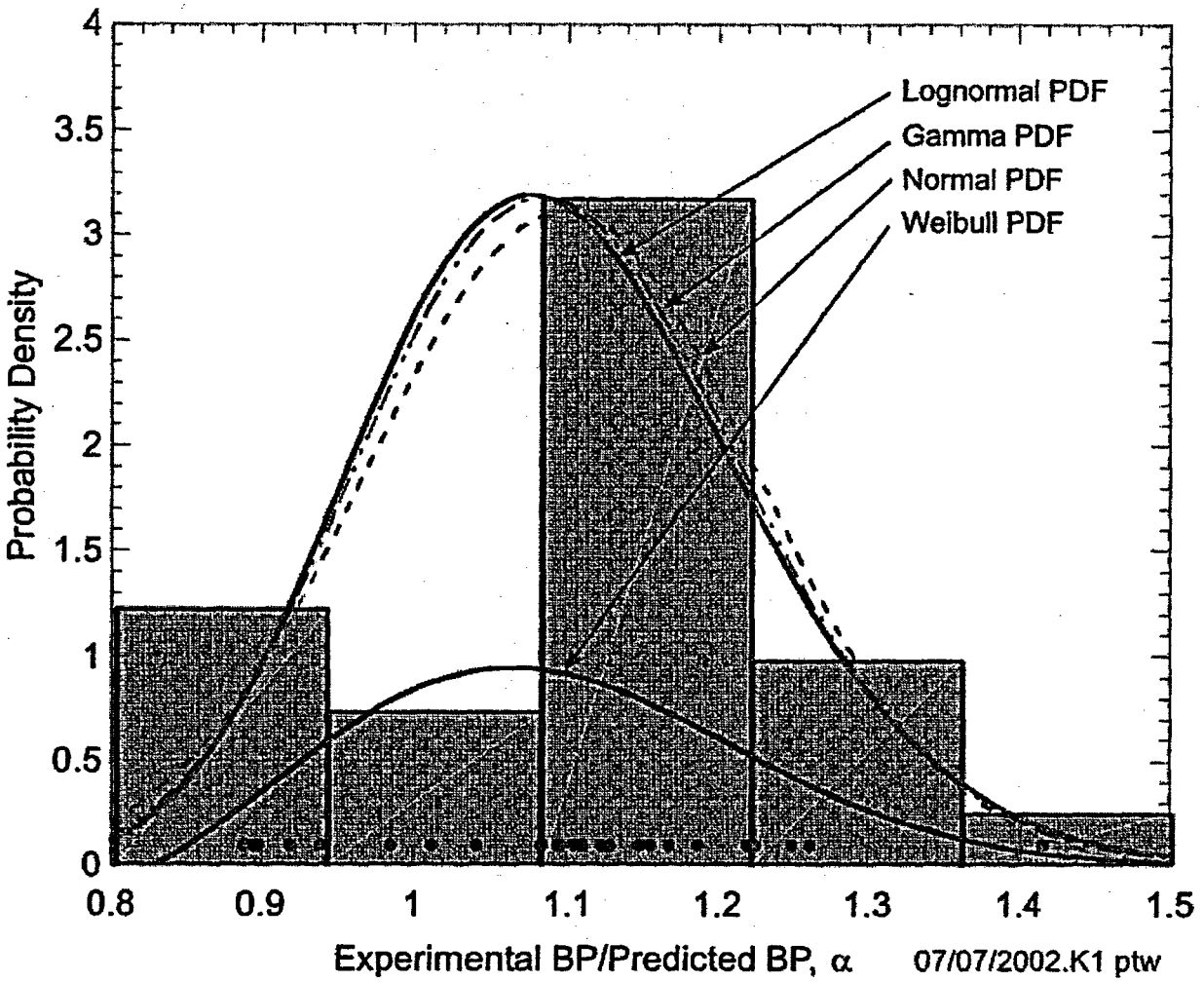

Fig. 7. Histogram of combined data set compared to probability densities of four fitted distributions.

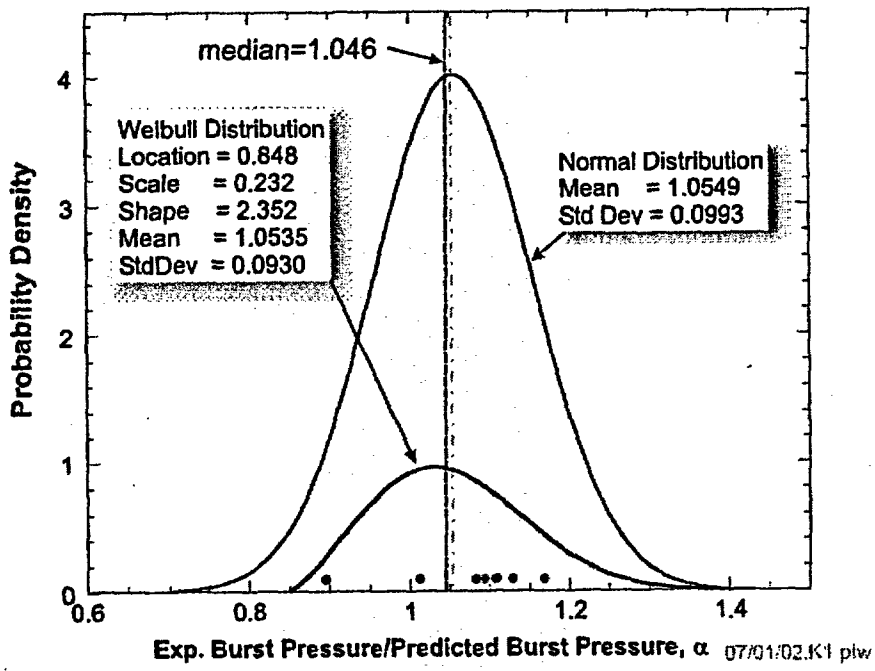

Fig. 8. Probability densities for two continuous statistical distributions fitted to the sample of 9 data points for α = experimental burst pressure/FEM predicted burst pressure.

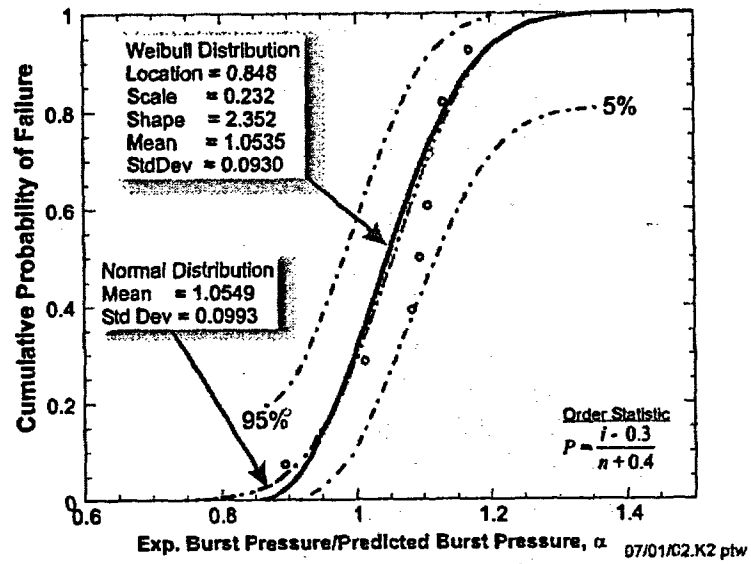

Fig. 9. Weibull statistical failure model ($n = 9$) compared to a normal cumulative distribution function, median rank order statistic, and the 90% confidence interval on the order statistic. ABAQUS FEM solutions were used to develop the models. N.B.: The order statistics and their 90% confidence intervals are shown here for comparative purposes only and were not used in the point-estimate procedures for the parameters of either the Weibull or normal distributions.

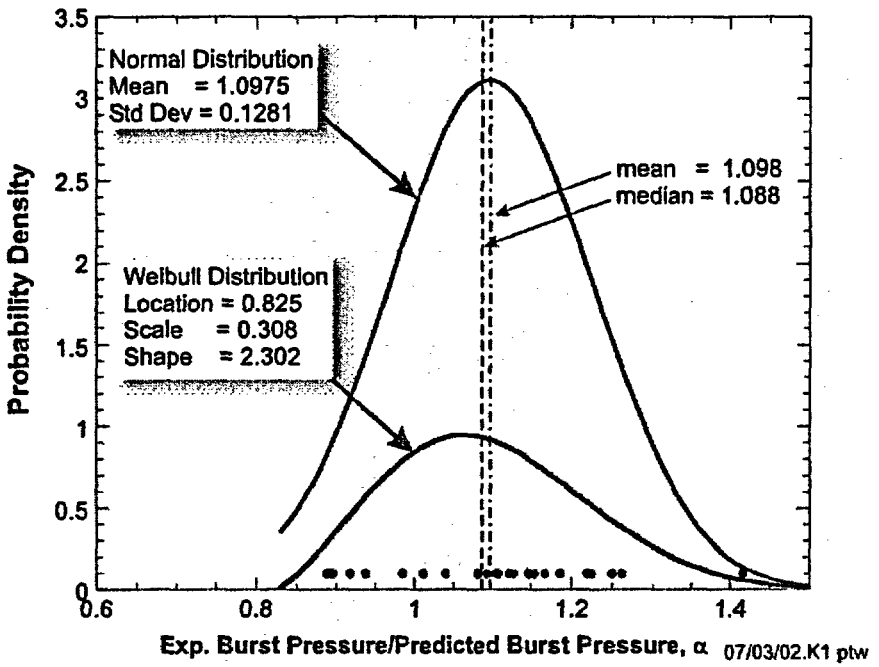

Fig. 10. Probability densities for two continuous statistical distributions fitted to the combined sample of 26 data points for α = experimental burst pressure / predicted burst pressure.

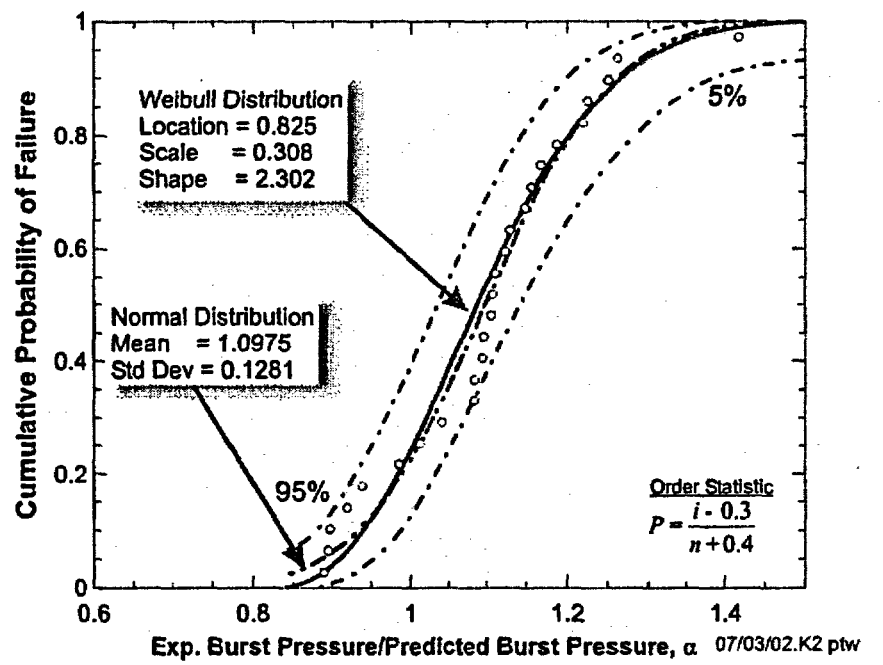

Fig. 11. Weibull statistical failure model (n = 26) compared to a normal cumulative distribution function, median rank order statistic, and the 90% confidence interval on the order statistic. Models developed with combined sample. N.B.: The order statistics and their 90% confidence intervals are shown here for comparative purposes only and were not used in the point-estimate procedures for the parameters of either the Weibull or Normal distributions.

The recommended Weibull stochastic model of failure has the following form

$$f_W(\alpha)=\begin{cases}\dfrac{2.302}{0.308}\left(\dfrac{\alpha-0.825}{0.308}\right)^{1.302}\exp\left[-\left(\dfrac{\alpha-0.825}{0.308}\right)^{2.302}\right], & (\alpha>0.825)\\ 0, & (\alpha\le 0.825)\end{cases}$$

$$\Pr(X\le\alpha)=\int_{-\infty}^{\alpha}f_W(\xi)d\xi=\begin{cases}1-\exp\left[-\left(\dfrac{\alpha-0.825}{0.308}\right)^{2.302}\right], & (\alpha>0.825)\\ 0, & (\alpha\le 0.825)\end{cases} \tag{22}$$

where α is the ratio of the true (but unknown) burst pressure to the calculated burst pressure. If nonzero estimates are required for values of $\alpha<0.825$, then the following normal distribution may be used

$$f_N(\alpha)=\frac{1}{0.1281\sqrt{2\pi}}\exp\left[-\frac{1}{2}\left(\frac{\alpha-1.0975}{0.1281}\right)^2\right],\ (-\infty<\alpha<\infty)$$

$$\Pr(X\le\alpha)=\frac{1}{0.1281\sqrt{2\pi}}\int_{-\infty}^{\alpha}\exp\left[-\frac{1}{2}\left(\frac{\xi-1.0975}{0.1281}\right)^2\right]d\xi,\ (-\infty<\alpha<\infty) \tag{23}$$

These models may also be considered as statistical estimates of the expected predictive accuracy of computational methods applied to burst pressure calculations for constrained diaphragms.

4. Application of Stochastic Model to Bounding Calculation

A bounding calculation was carried out for the "as-found" condition of the wastage area in the Davis-Besse head. The finite-element model used in the analysis is shown in Fig. 12. An adjusted stress-strain curve (see Fig. 13) was constructed to lower-bound the available data for the cladding material. The geometry of the wastage area footprint was taken from Fig. 13 in the *Root Cause Analysis Report* [12]. As an estimate of the uncertainty in the current wastage area measurements, the footprint was extended by approximately 0.25 inches (see Table 10 and Fig. 14 for a geometric description of the adjusted footprint). A uniform cladding thickness of 0.24 inches (the minimum cladding thickness value shown in Fig. 14 of ref. [12]) was assumed in the model. The finite-element model was then loaded with increasing pressure until the point of numerical instability at an internal pressure of 6.65 ksi (see Fig. 15).

For the predicted burst pressure of 6.65 ksi, the normal and Weibull statistical failure models can be scaled to provided estimates of cumulative probability of failure as a function of internal service pressure for the specific condition of the wastage area simulated by the finite-element analysis. Examples of the scaled Weibull model are shown in Figs. 16 and 17 for normalized internal pressure and direct internal pressure, respectively. The scaled Weibull model has the form

$$f_W(P\,|\,P_{BP}) = \frac{2.302}{P_{BP}\times 0.308}\left(\frac{P-P_{BP}\times 0.825}{P_{BP}\times 0.308}\right)^{1.302}\exp\left[-\left(\frac{P-P_{BP}\times 0.825}{P_{BP}\times 0.308}\right)^{2.302}\right],(P>P_{BP}\times 0.825)$$

$$\Pr\left(P_{BP(true)}\le P\,|\,P_{BP}\right) = \begin{cases} 1-\exp\left[-\left(\frac{P-P_{BP}\times 0.825}{P_{BP}\times 0.308}\right)^{2.302}\right], & (P>P_{BP}\times 0.825) \\ 0 & ,(P\le P_{BP}\times 0.825) \end{cases} \tag{24}$$

where P_{BP} is the predicted burst pressure (either normalized by the operating pressure or in dimensional form), and $P_{PB(true)}$ is the unknown true burst pressure. The scaled normal distribution is

$$f_N(P\,|\,P_{BP}) = \frac{1}{P_{BP}\times 0.1281\sqrt{2\pi}}\exp\left[-\frac{1}{2}\left(\frac{P-P_{BP}\times 1.0975}{P_{BP}\times 0.1281}\right)^2\right]$$

$$\Pr\left(P_{BP(true)}\le P\,|\,P_{BP}\right) = \frac{1}{P_{BP}\times 0.1281\sqrt{2\pi}}\int_{-\infty}^{P}\exp\left[-\frac{1}{2}\left(\frac{\xi-P_{BP}\times 1.0975}{P_{BP}\times 0.1281}\right)^2\right]d\xi \tag{25}$$

Table 10. Wastage-Area-Footprint Geometry Data

Description	Scaling Factor	Area	Perimeter	Centroid of Wastage Area Footprint		Moments of Inertia About the Centroid			Eigenvalue Extraction for Principal Moments and Directions			
				x_c	y_c	I_{xx}	I_{yy}	I_{xy}	Principal Moments I_1	I_2	Principal Directions I_1	I_2
		(in²)	(in.)	(in.)	(in.)	(in⁴)	(in⁴)	(in⁴)	(in⁴)	(in⁴)	$< n_x, n_y >$	$< n_x, n_y >$
As-Found Footprint	1	35.36	30.36	16.4122	-0.1194	98.89	9699.33	-117.16	75.26	197.41	<0.9004, -0.4351>	<0.4351, 0.9004>
Adjusted Footprint for Bounding Calculation	0.25 in.	40.06	31.78	16.4301	-0.1255	129.02	11031.81	-141.35	99.00	245.71	<0.8943, -0.4476>	<0.4476, 0.8943>

Footprint centroid is in global coordinates.
Global coordinate system has its z-axis aligned with the vertical centerline of the vessel.
The x-y plane of the global coordinate system is a horizontal plane
with the x-axis along the line between the centerlines of Nozzles 3 and 11.

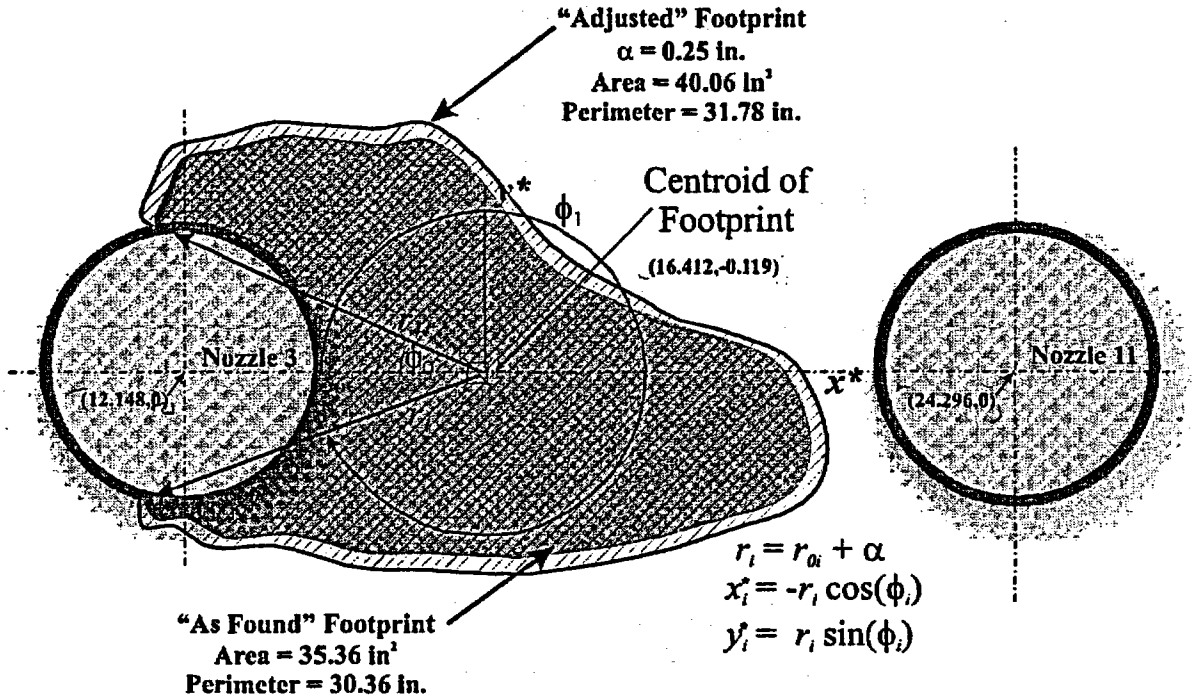

Table 10 (continued) Details of Wastage Area Footprint Before Adjustment for Bounding Calculation (Figure taken from Fig. 13 ref. [12])

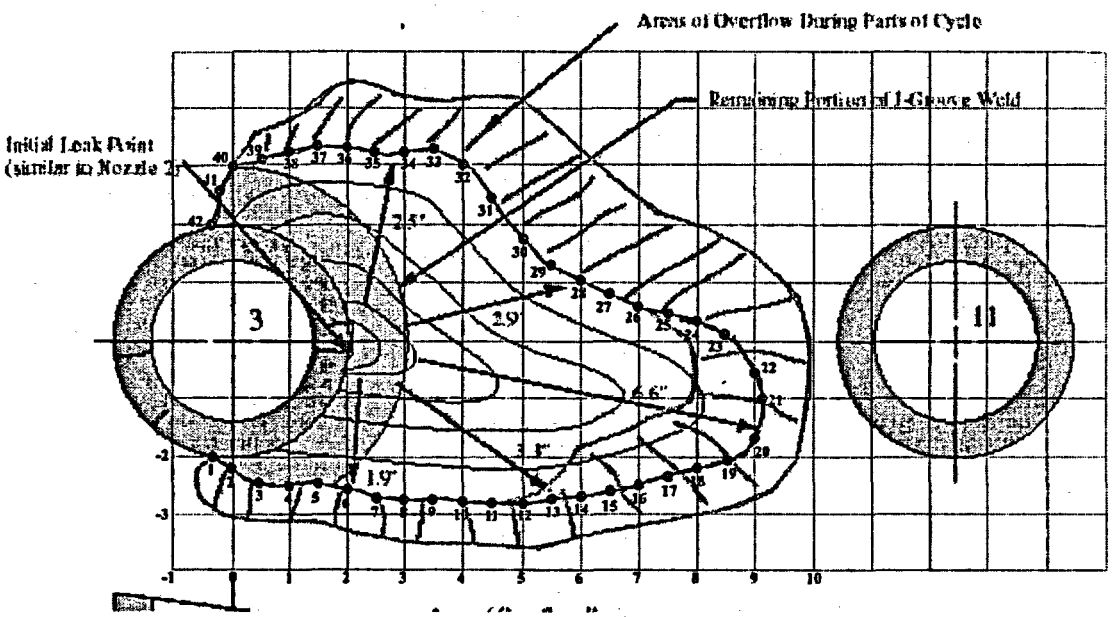

Point	x*	y*	Point	x*	y*
0	-0.639	-1.895	24	8.000	0.334
1	-0.334	-2.280	25	7.500	0.483
2	0.000	-2.235	26	7.000	0.582
3	0.500	-2.492	27	6.500	0.829
4	1.000	-2.522	28	6.000	1.046
5	1.500	-2.482	29	5.500	1.303
6	2.000	-2.581	30	5.000	1.778
7	2.500	-2.730	31	4.500	2.460
8	3.000	-2.769	32	4.000	3.023
9	3.500	-2.759	33	3.500	3.300
10	4.000	-2.789	34	3.000	3.221
11	4.500	-2.819	35	2.500	3.250
12	5.000	-2.819	36	2.000	3.300
13	5.500	-2.759	37	1.500	3.349
14	6.000	-2.700	38	1.000	3.240
15	6.500	-2.621	39	0.500	3.122
16	7.000	-2.512	40	0.000	3.000
17	7.500	-2.364	41	-0.210	2.578
18	8.000	-2.216	42	-0.364	2.000
19	8.500	-2.087	43	-0.242	1.985
20	9.000	-1.712			
21	9.135	-1.000			
22	9.000	-0.555			
23	8.500	0.137			

Origin of local coordinate system located at centerline of Nozzle 3. (inches)

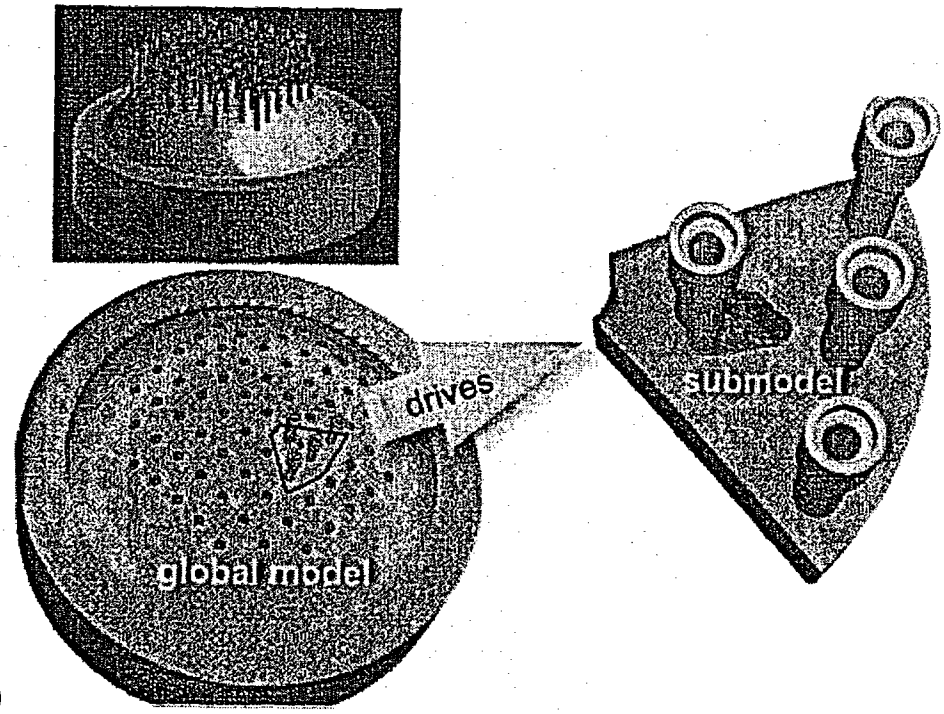

(a)

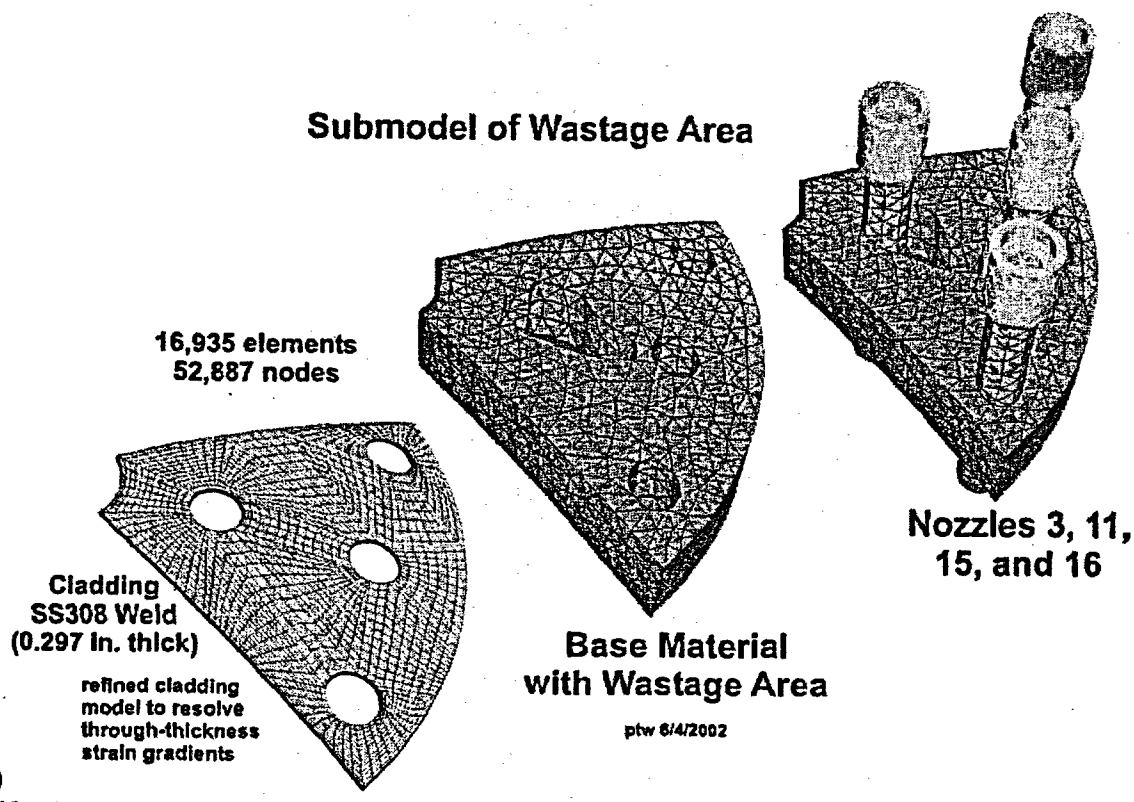

(b)

Fig. 12. Finite-element global and submodels of the Davis-Besse head and wastage area. The displacements at the vertical side boundaries of the submodel are driven by the global model. Both models are exposed to the same internal pressure loading.

(c)

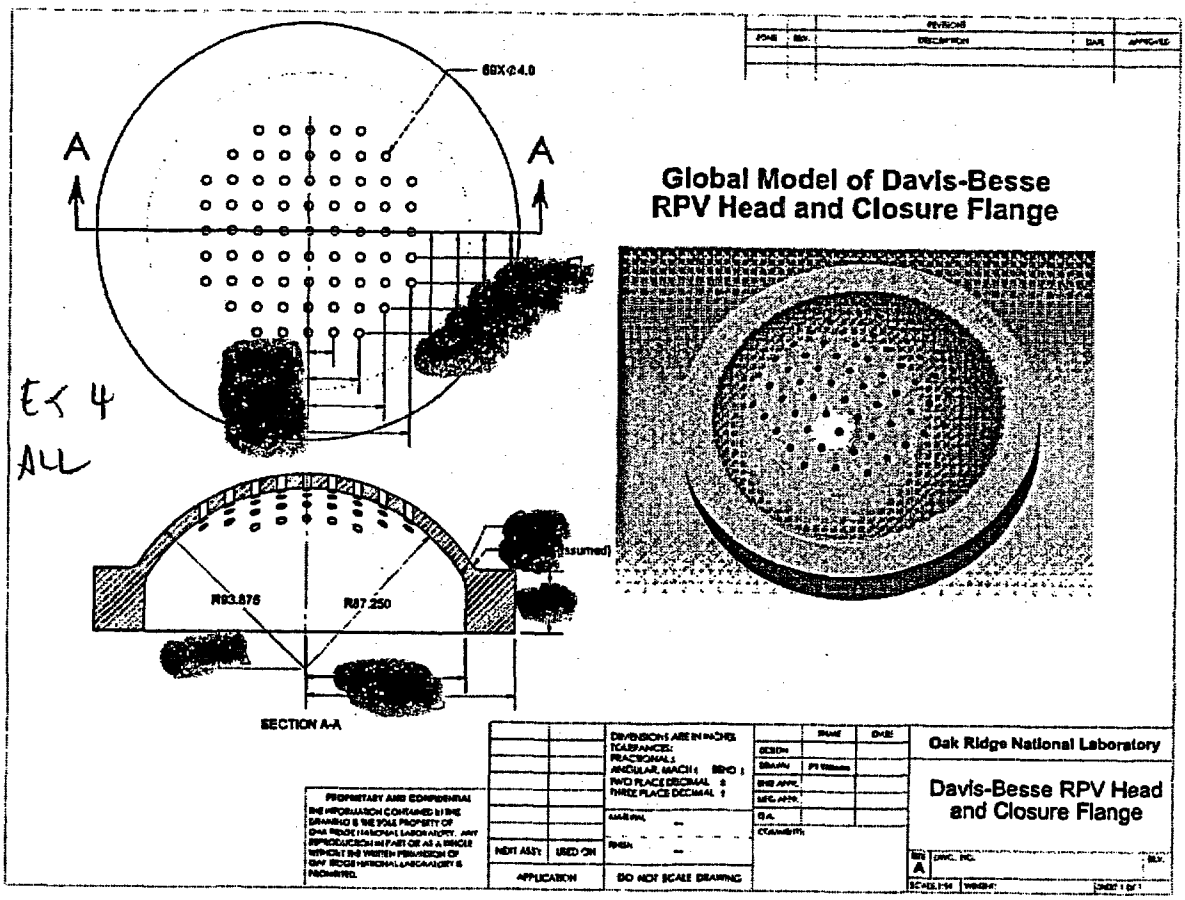

Fig 12 (continued) (c) geometry of RPV head and closure flange used in global model,

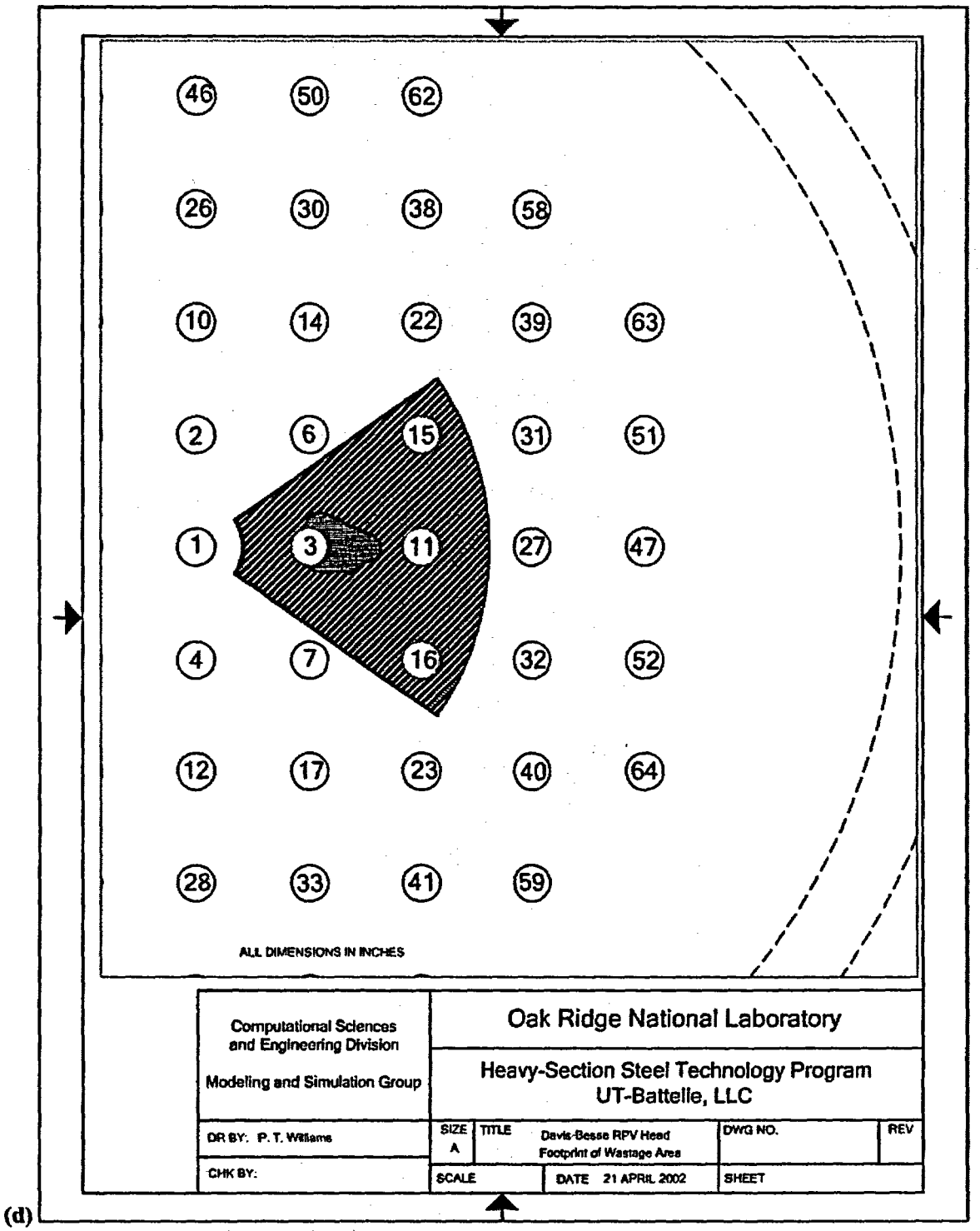

(d)

Fig 12 (continued) (d) relative location of submodel within full RPV head,

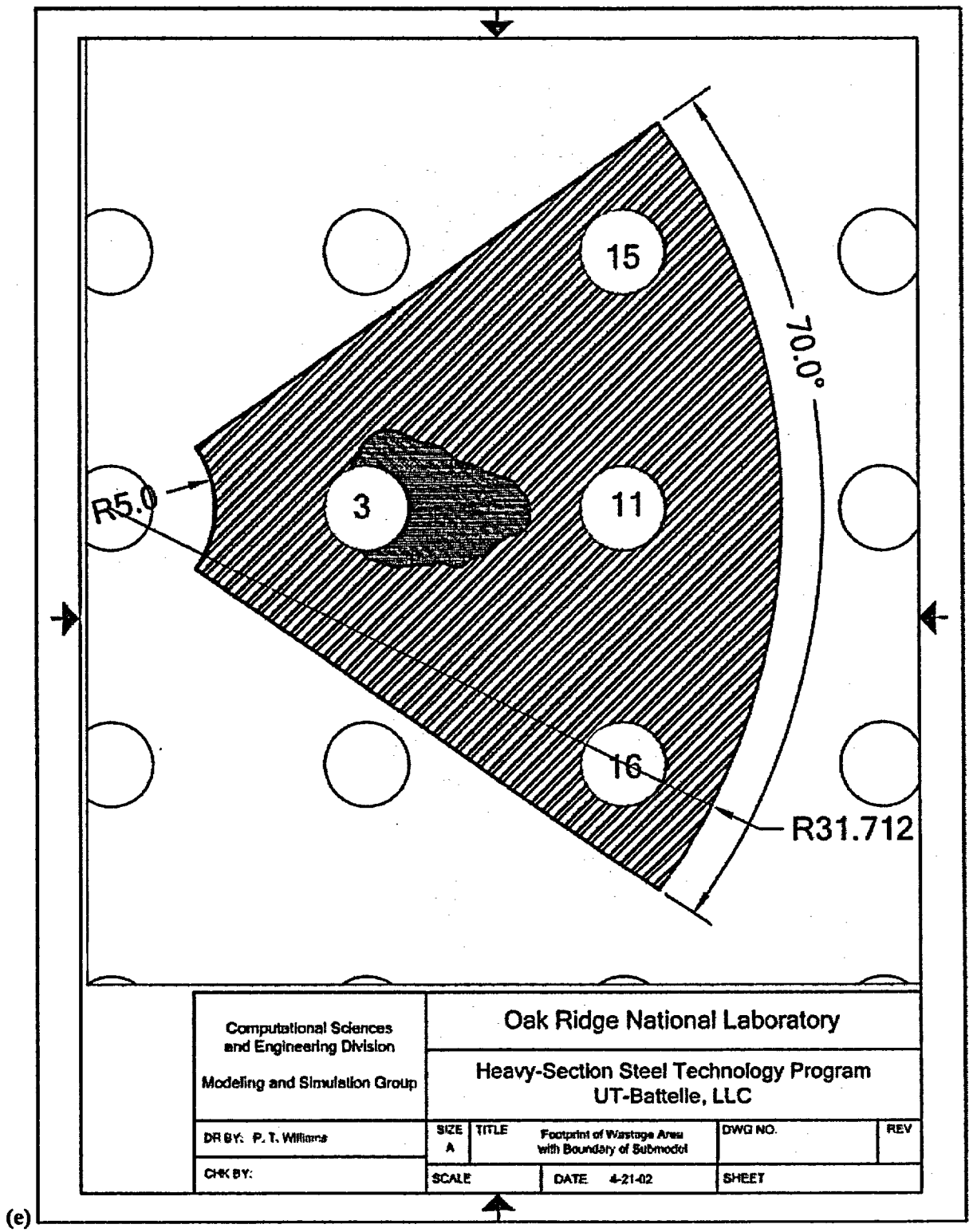

(e)

Fig 12 (continued) (e) geometry of submodel relative to Nozzles 3, 11, 15, and 16.

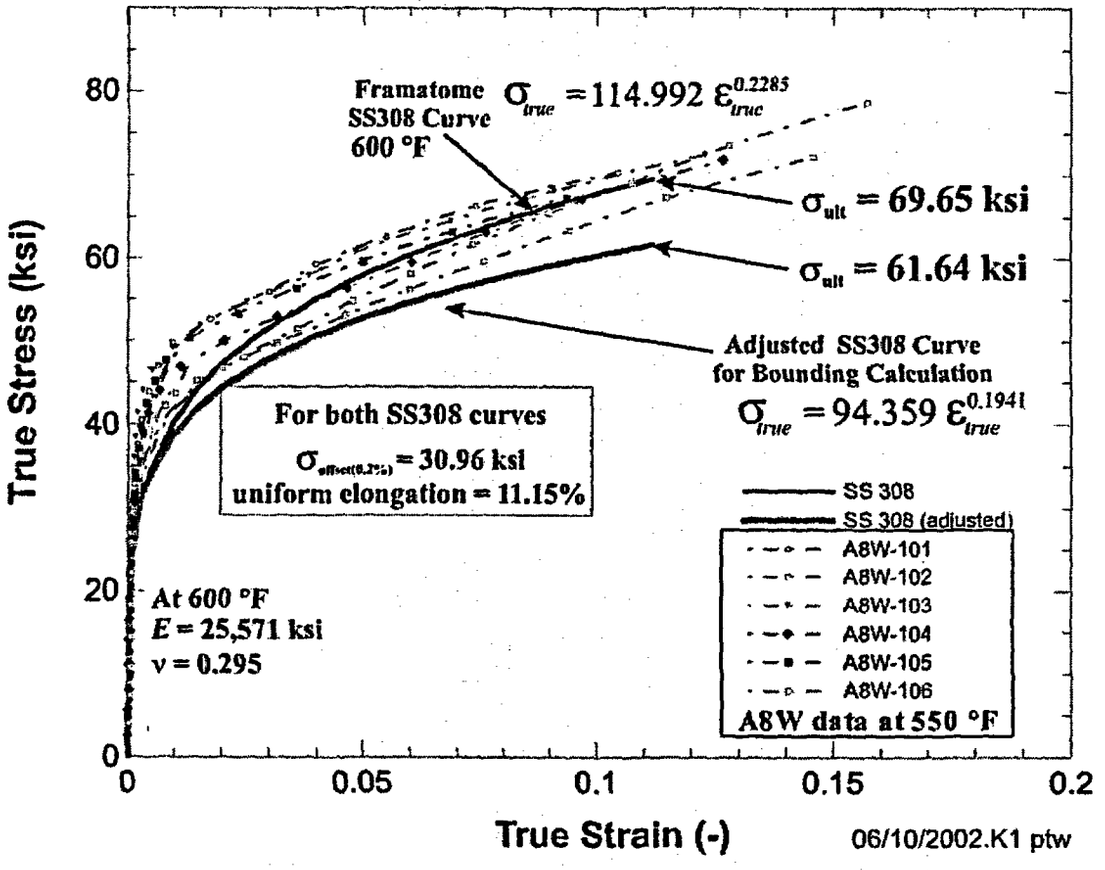

Fig. 13. Adjusted SS308 stress vs. strain curve used in the bounding-case calculations compared to curves from a range of A8W heats. Strain hardening in the adjusted curve was reduced to lower-bound all of the data. The offset yield strength and strain at ultimate strength were retained from the unadjusted SS308 curve received from Framatome.

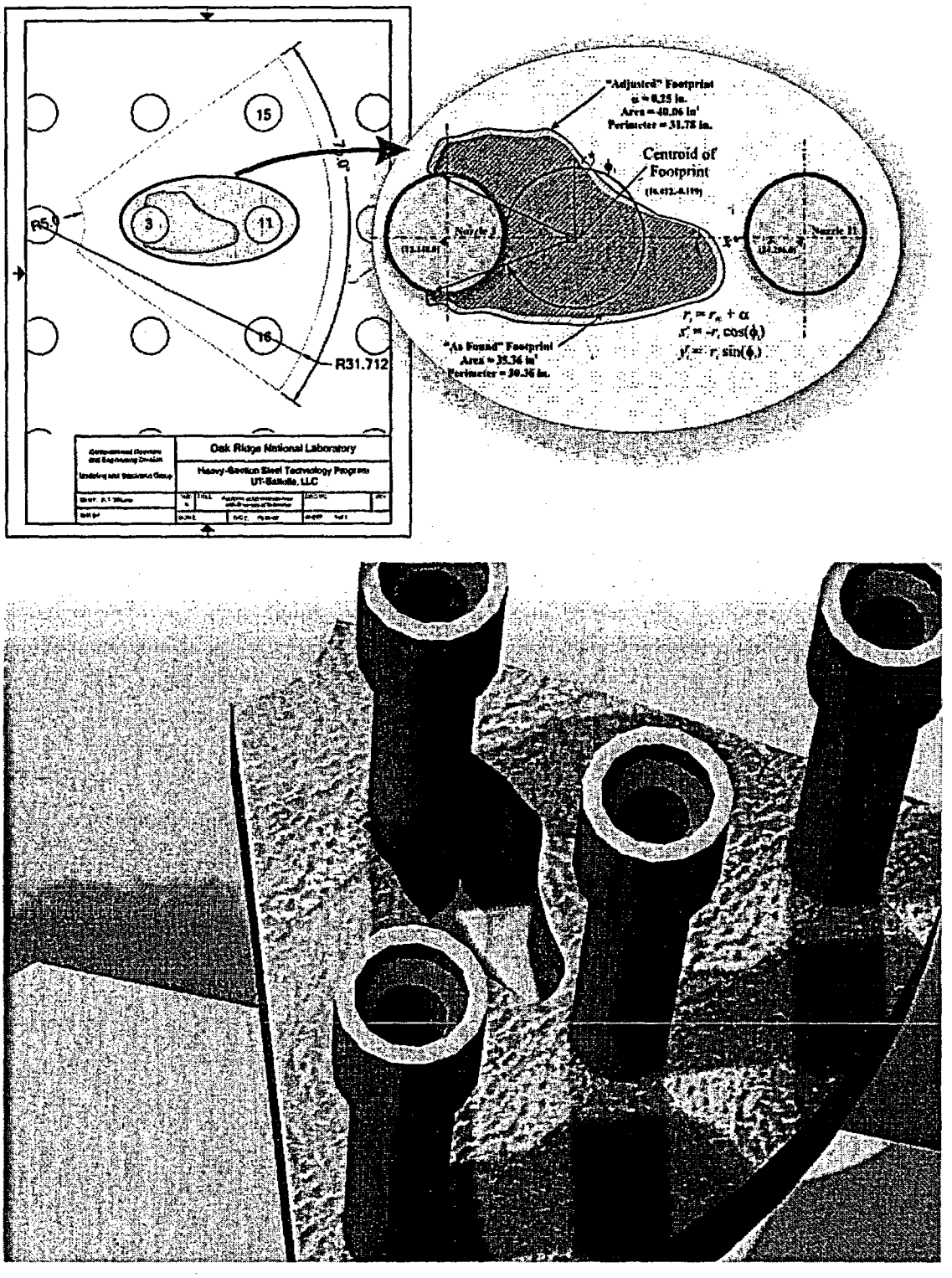

Fig. 14. Geometry of adjusted wastage area footprint. Lower figure is a Photoworks®-rendered image of the submodel with the adjusted "as-found" footprint.

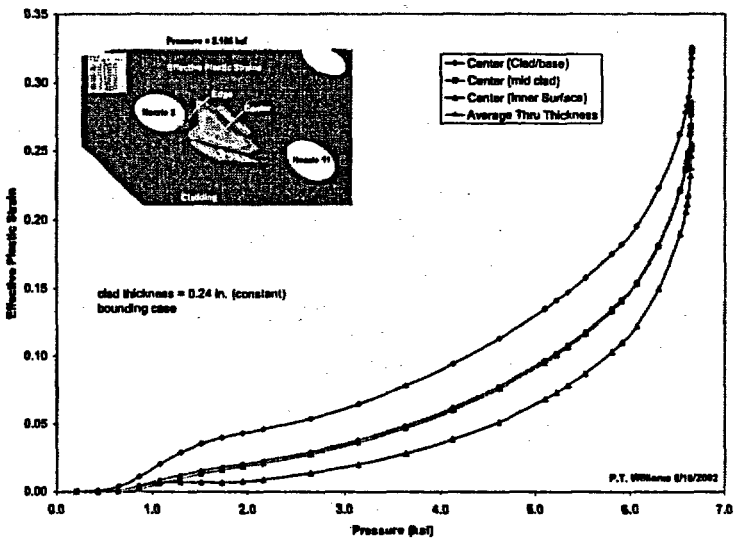

(a)

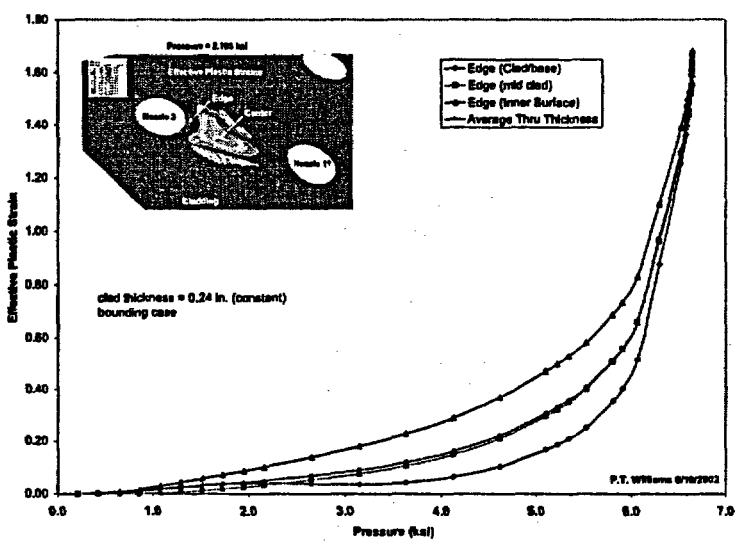

(b)

Fig. 15. Effective plastic-strain histories at two high-strain locations in the wastage area: (a) near the center and (b) near Nozzle 3.

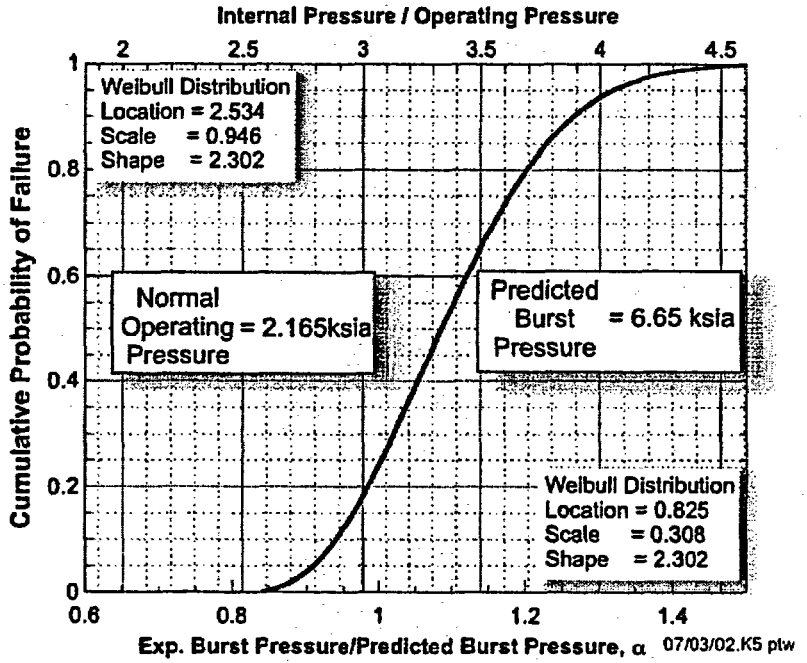

Fig. 16. Application of the failure statistical criterion produces a cumulative probability of failure (based on a Weibull distribution) curve for the Bounding Case condition. Cumulative probability of failure as a function of normalized internal pressure.

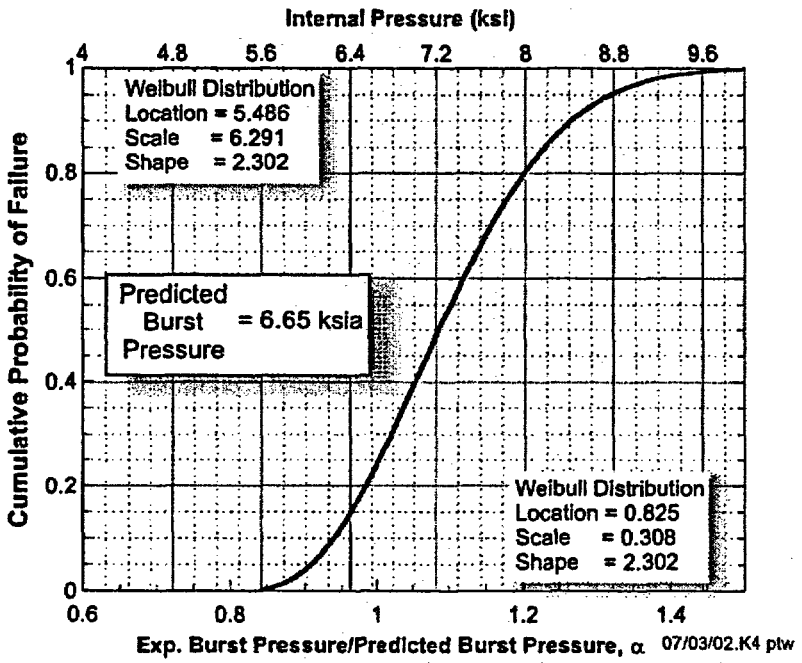

Fig. 17. Application of the failure statistical criterion produces a cumulative probability of failure (based on a Weibull distribution) curve for the Bounding Case condition. Cumulative probability of failure as a function of internal pressure.

As discussed above, the bounding calculation predicted a burst pressure of 6.65 ksi which has a cumulative probability of failure of 0.244. For pressures below 5.486 ksi (at the position of the location parameter), the Weibull model predicts a zero probability of failure. The model based on a normal distribution estimates a cumulative probability of failure of 8.43×10^{-10} at the operating pressure of 2.165 ksi and 8.89×10^{-9} at 2.5 ksi. See Table 11 for additional estimates.

Table 11. Estimated Cumulative Probability of Failures for the Bounding Calculation

Internal Pressure (ksi)	Normal Cumulative Probability of Failure	Weibull Cumulative Probability of Failure
2.155	7.84E-10	0
2.165	8.43E-10	0
2.200	1.09E-09	0
2.225	1.30E-09	0
2.250	1.55E-09	0
2.275	1.86E-09	0
2.300	2.22E-09	0
2.325	2.65E-09	0
2.350	3.15E-09	0
2.375	3.76E-09	0
2.400	4.47E-09	0
2.425	5.32E-09	0
2.450	6.32E-09	0
2.475	7.50E-09	0
2.500	8.89E-09	0

5. Summary and Conclusions

A stochastic model of the probability of failure associated with a computational prediction of the plastic collapse of the exposed cladding in the wastage area of the Davis-Besse RPV head has been developed from the following technical bases:

(5) *experimental data* obtained during disk-burst tests reported by Riccardella [2] with loadings, geometries, and materials relevant to the Davis-Besse pressure loading, wastage-area footprint, and cladding,

(6) nonlinear, large-deformation, elastic-plastic *discrete-element analyses* of the disk-burst tests also reported in [2] (GAPL-3 discrete-element code[3]),

(7) nonlinear, finite-strain, elastic-plastic *finite-element analyses* performed for the current study (ABAQUS finite-element code[4]) of the nine disk-burst test specimens reported in [2], and

(8) a *theoretical criterion* for plastic instability in a circular diaphragm under pressure loading, due to Hill [5] (as cited in [6]), applied to the disk-burst tests.

The final Weibull model has the scaled form of

$$\Pr\left(P_{BP(true)} \le P\right) = F_W(P \mid P_{BP}) = \begin{cases} 1-\exp\left[-\left(\dfrac{P-P_{BP}\times 0.825}{P_{BP}\times 0.308}\right)^{2.302}\right], & (P > P_{BP}\times 0.825) \\ 0, & (P \le P_{BP}\times 0.825) \end{cases} \qquad (26)$$

Given a computationally predicted burst pressure, P_{BP}, the model gives an estimate of the cumulative probability that the true but unknown burst pressure $P_{BP(true)} \le P$, where P is the service pressure under consideration. A normal distribution is also available for nonzero failure-probability estimates at pressures below the location parameter in the Weibull distribution.

As an example application, estimates are provided for a bounding calculation of the "as-found" Davis-Besse wastage area. The bounding calculation predicted a burst pressure of 6.65 ksi which has a cumulative probability of failure of 0.244. For pressures below 5.486 ksi (at the position of the location parameter), the Weibull model predicts a zero probability of failure. The model based on a normal distribution estimates a cumulative probability of failure of 8.43×10^{-10} at the operating pressure of 2.165 ksi and 8.89×10^{-9} at 2.5 ksi.

References

1. *Recent Experience with Degradation of Reactor Pressure Vessel Head,* NRC Information Notice 2002-11, United States Nuclear Regulatory Commission, Office of Nuclear Reactor Regulation, Washington, DC, March 12, 2002.
2. P. C. Riccardella, "Elasto-Plastic Analysis of Constrained Disk Burst Tests," Paper No. 72-PVP-12, presented at the ASME *Pressure Vessels and Piping Conference,* September 17-21, 1972, New Orleans, LA.
3. A. L. Thurman, *GAPL-3-A Computer Program for the Inelastic Large Deflection Stress Analysis of a Thin Plate or Axially Symmetric Shell with Pressure Loading and Deflection Restraints,* WAPD-TM-791, Bettis Atomic Power Laboratory, Pittsburgh, PA, June 1969.
4. *ABAQUS/Standard User's Manual, v. 6.2,* Hibbit, Karlsson, and Sorensen, Inc., Pawtucket, RI, 2001.
5. R. Hill, "A Theory of the Plastic Bulging of a Metal Diaphragm by Lateral Pressure," *Philos. Mag. (Ser. 7)* **41**, (1950) 1133.
6. A. R. Ragab and S. E. Bayoumi, *Engineering Solid Mechanics, Fundamentals and Applications,* CRC Press LLC, Boca Raton, FL, 1999.
7. W. E. Cooper, E. H. Kotteamp, and G. A. Spiering, "Experimental Effort on Bursting of Constrained Disks as Related to the Effective Utilization of Yield Strength," Paper No. 71-PVP-49, ASME *Pressure Vessels and Piping Conference,* May 1971.
8. J. Chakrabarty and J. M. Alexander, "Hydrostatic Bulging of Circular Diaphragms," *J. Strain Anal.* 5(3), (1970) 155-161.
9. *GenStat® Release 6.1 Reference Manual,* VSN International, Oxford, UK, 2002.
10. M. A. Stephens, "EDF Statistics for Goodness of Fit and Some Comparisons," *Journal of the American Statistical Association* 69 (1974), 730-737.
11. J. A. Aitchison, *The Statistical Analysis of Compositional Data,* Chapman and Hall, London, 1986.
12. S. A. Loehlein, *Root Cause Analysis Report, Significant Degradation of Reactor Pressure Vessel Head,* CR 2002-0891, Davis-Besse Power Station, April 15, 2002.

Appendix A – Statistical Point-Estimation Techniques for Weibull Distributions

The three parameters for the Weibull distributions of α (=experimental burst pressure/predicted burst pressure) were calculated using a combination of two point-estimation procedures, *Maximum Likelihood* and the *Method of Moments*. The parameters to estimate are the location parameter, a, of the random variate, the scale parameter, b, of the random variate, and the shape parameter, c.

Maximum likelihood estimators for the shape parameter c' and the scale parameter b' can be derived from the likelihood function, L, for the Weibull distribution. The Weibull density is given by

$$w(\alpha|a,b,c) = \frac{c}{b} y^{c-1} \exp\left(-y^c\right), \text{ for } (y = (\alpha - a)/b, \alpha > a,\ b,c > 0) \tag{A.1}$$

and the corresponding likelihood function is the joint density (see Ref.[A1]) (given the location parameter, a)

$$L(b,c\,|\,\alpha,a) = \prod_{i=1}^{N} \frac{c}{b}\left(\frac{\alpha_{(i)} - a}{b}\right)^{c-1} \exp\left[-\left(\frac{\alpha_{(i)} - a}{b}\right)^{c}\right] \tag{A.2}$$

The maximum likelihood (*ML*) estimators for the scale, b', and shape parameters, c', are defined as the unique values of (b',c') that maximize the joint probability that the N members of the sample set all come from the same parent population. The *ML* estimators are, therefore, calculated by finding the stationary point of Eq. (A.2). Upon taking the logarithm of Eq. (A.2), the derivatives with respect to the individual parameters (b',c') are set to zero. The resulting *ML* estimator for the shape parameter, c', is found by solving iteratively for c' in the following nonlinear equation

$$\frac{\partial(\ln(L(c')))}{\partial c'} = \frac{\sum_{i=1}^{N} (\alpha_{(i)} - a)^{c'} \ln(\alpha_{(i)} - a)}{\sum_{i=1}^{N} (\alpha_{(i)} - a)^{c'}} - \frac{1}{N}\sum_{i=1}^{N} \ln(\alpha_{(i)} - a) - \frac{1}{c'} = 0 \tag{A.3}$$

Upon obtaining a solution for c', the *ML* estimator for the scale parameter, b', follows directly from

$$\frac{\partial(\ln(L))}{\partial b'} = b' - \left[\sum_{i=1}^{N} \frac{(\alpha_{(i)} - a)^{c'}}{N}\right]^{\frac{1}{c'}} = 0 \tag{A.4}$$

For the *ML* point estimators for (b', c'), the location parameter, a, was assumed given.

The *Method of Moments* (*MM*) can now be applied to provide a point estimate for the location parameter, a^*. In the *Method of Moments*, the sample moments are used as estimators for the population moments. The *MM* point estimator for the scale parameter, b^*, is (given the shape parameter, c),

$$b^* = \sqrt{m_2 / [\Gamma(1+2/c) - \Gamma^2(1+1/c)]} \tag{A.5}$$

where m_2 is the second moment of the sample about the sample mean and Γ is Euler's gamma function. The *MM* estimator for the location parameter, a^*, follows from

$$a^* = m_1' - b^* \Gamma(1+1/c) \tag{A.6}$$

where m_1' is the 1st crude moment of the sample (the sample mean) and the sample moments are defined by

$$\begin{aligned} m_1' &= \sum_{i=1}^{N} \frac{\alpha_{(i)}}{N} \\ m_2 &= \sum_{i=1}^{N} \frac{(\alpha_{(i)} - m_1')^2}{N} \end{aligned} \tag{A.7}$$

From Ref. [B.2], a moment estimator for the shape parameter, c^*, also exists

$$c^* = \frac{4.104683 - 1.148513\sqrt{b_1} + 0.44326(\sqrt{b_1})^2 - 0.053025(\sqrt{b_1})^3}{\sqrt{b_1} + 1.139547} \tag{A.8}$$

where $\sqrt{b_1}$ is the sample skewness. However, for sample sizes as small as 20, there will be a high level of uncertainty in the (a^*, b^*, c^*) estimates derived from c^* (Ref. [A.2]).

The three parameters for the Weibull distribution of α were estimated through the following iterative sequence:

1. For the discrete set $(\alpha_{(i)}, i = 1, N)$, calculate the sample moments, (m_1', m_2) from Eqs. (A.7).
2. Select a trial value for the location parameter, a_{trial} where $a_{trial} < \min(\alpha_{(i)}, i = 1,2,\ldots N)$.
3. Calculate *ML* estimates for (c', b') from Eqs. (A.3)-(A.4) by letting $a = a_{trial}$.
4. Calculate MM estimates for (a^*, b^*) from Eqs. (A.5)-(A.6) by letting $c = c'$ as determined in Step 3.
5. Calculate a relative deviation between the trial a_{trial} and the MM estimate of a^* from Step 4 by

$$\delta = \frac{a_{trial} - a^*}{a_{trial}} \tag{A.9}$$

6. Given $\varepsilon_{tolerance}$, as a pre-selected convergence tolerance, if $\delta > \varepsilon_{tolerance}$, then select a new trial location parameter, a_{trial}, and repeat Steps 3-6 until convergence, defined as $\delta \le \varepsilon_{tolerance}$.

Upon convergence, there will be two triplets (a_{trial}, b', c') and (a^*, b^*, c') where in general $a_{trial} \approx a^*$ and $b' \neq b^*$ although b' was typically close to b^* in this study. The triplet (a^*, b', c') was taken as the converged estimate for the parameters of the Weibull distribution for α.

References

A1. A. Ghosh, "A FORTRAN Program for Fitting Weibull Distribution and Generating Samples," *Computers & Geosciences* **25**, (1999) 729-738.

A2. K. O. Bowman and P. T. Williams, *Technical Basis for Statistical Models of Extended K_{Ic} and K_{Ia} Fracture Toughness Databases for RPV Steels*, ORNL/NRC/LTR-99/27, Oak Ridge National Laboratory, Oak Ridge, TN, February 2000.